Geochimica et Cosmochimica Acta 388 (2025) 18–33

Contents lists available at ScienceDirect

Geochimica et Cosmochimica Acta

journal homepage: www.elsevier.com/locate/gca

Layer-to-tunnel manganese oxides transformation triggered by pyrogenic carbon and trace metals: Key role of reducing and oxidizing components cooperation

Zibo Xu [a], Bin Ma [b], Yuanzhi Tang [c], Daniel C.W. Tsang [a,*]

[a] Department of Civil and Environmental Engineering, The Hong Kong University of Science and Technology, Clear Water Bay, Hong Kong, China
[b] Laboratory for Waste Management, Nuclear Energy and Safety, Paul Scherrer Institute, 125232 Villigen, Switzerland
[c] School of Earth and Atmospheric Sciences, Georgia Institute of Technology, 311 Ferst Dr, Atlanta, GA 30332, USA

ARTICLE INFO

Associate editor: Juan Liu

Keywords:
Pyrogenic carbon
Toxic elements
Mineral transformation
Electron transfer
Manganese oxides

ABSTRACT

Manganese oxide (MnO_x) plays crucial roles in shaping various environmental and geochemistry processes, with their reactivity largely dependent on the structure of MnO_x. Tunnel MnO_x effectively hosts a substantial quantity of soil elements within its tunnel structure, exerting significant control over element turnover and pertinent geochemical processes, while the precise determinants regarding the layer-to-tunnel transformation of MnO_x with electron transfer remain unclear. In this study, we delved into the transformation of layer-structured MnO_x during the interaction with coexisting soil redox components (pyrogenic carbon and Tl with differing redox reactivity). Our findings revealed that the transformation from layer to tunnel structure only occurred in the presence of reductive pyrogenic carbon and oxidative Tl(III) rather than sole reductants/oxidants within a short incubation period of 6 weeks. The macro reducing environment created by the pyrogenic carbon and the micro oxidizing environment related to the Tl(III) chelation was pivotal in the cyclic valence change of Mn, resulting in the generation of Mn(III) and vacancies in the Mn structure, the prerequisite for the layer-to-tunnel transformation. Anchoring of oxidative Tl(III) on the surface or inside the tunnel structure of MnO_x through Tl–O–Mn bonding was the key to building a micro oxidative environment under bulk-reducing conditions. During the transformation, Tl was integrated into the tunnel of high-crystallinity MnO_x, and prolonged incubation resulted in the deeper embedding of Tl and the formation of atomic clusters. The embedding of Tl inside of the tunnel MnO_x led to lower solubility and bioaccessibility, with only 0.05–0.26 mg Kg^{-1} being extracted with soil organic acids through reductive dissolution and 8.7–8.9 % by in vitro physiologically based extraction test. This study underscores the significant role of electron-donating and electron-accepting components in triggering interconnected geochemical processes with MnO_x, carbon, and trace elements.

1. Introduction

Manganese (Mn) constitutes the second most prevalent transition metal at a range of 0.09–0.11 %, and Mn oxides (MnO_x) represent a potent group of mineral oxidants within the Earth's crust. MnO_x is pivotal in the geochemical cycling of various elements, including carbon (Brüggenwirth et al., 2024; Moore et al., 2023), nitrogen (Karolewski et al., 2021), phosphorus (Chen et al., 2022), iron (Liu et al., 2021), halogen (Du et al., 2023), and toxic metals (Flynn & Catalano, 2019; Phillips et al., 2023). The reactivity of Mn minerals is controlled by both valence state (+2 to + 4) (Zhang et al., 2023) and structural difference (Wu et al., 2021). For instance, generating Mn(III)-rich edges on the layer MnO_x might block the reactive vacancy sites, and Mn(II) formed by the MnO_x reduction might occupy the sorption sites (Flynn & Catalano, 2019). Both processes affect the mobilization of toxic elements (*e.g.*, Ni and Zn) in soils and aquatic systems. The layer-to-tunnel transformation of MnO_x was reported to either decrease or increase the mobility of toxic elements (Atkins et al., 2016; Wu et al., 2021). Thus, the intricate transformation of Mn minerals in conjunction with redox reactions constitutes a cornerstone in comprehending the elemental turnover and the eco-functionality of soil (Flynn & Catalano, 2019; Mock et al., 2019).

The dissolution of hexagonal phyllo-manganates with the formation of soluble Mn(II) represents pivotal stages in initiating reductive Mn transformation (Elzinga, 2011). For instance, reductants such as Fe(II)

* Corresponding author.
E-mail address: cedan@ust.hk (D.C.W. Tsang).

https://doi.org/10.1016/j.gca.2024.11.015
Received 21 June 2024; Accepted 15 November 2024
Available online 19 November 2024

(Limmer et al., 2023), Mn(II) (Zhao et al., 2018), and fulvic acid (Wang et al., 2018) show the potential to trigger the transformation of hexagonal MnO_2 to Mn_3O_4, MnOOH (Wang et al., 2019; Wang et al., 2018; Zhao et al., 2018), and $MnCO_3$ (Limmer et al., 2023). A higher reductant content (*e.g.,* fulvic acid to MnO_2 ratio > 1) invariably yields an augmented Mn(II) quantity and engenders the creation of lower-valence Mn minerals (*e.g.,* Mn_3O_4) within a compressed timeframe (24 h) (Wang et al., 2018). Another typical MnO_x transformation pathway encompasses topotactic variation as layer-to-tunnel transformation, frequently observed under high acidity in conjunction with toxic elements such as Tl(I) (Ruiz-Garcia et al., 2021), Cr(III) (Aiken et al., 2023), and Co(II) (Wu et al., 2021). The generation of Mn(II)/Mn(III) on the layer-structured MnO_x has equally deemed the inaugural phase in instigating the transformation, as an elevated reductant concentration customarily fosters the generation of tecto-manganates (Ruiz-Garcia et al., 2021; Yang et al., 2018). The tunnel MnO_x normally showed high importance for the fate of alkali, alkaline earth, transition, and rare earth metals, and they are common Mn minerals occurring in soil, sediments, and ocean floor (Post, 1999; Yang et al., 2018).

The precise determinants of layer-to-tunnel transformation of MnO_x remain elusive. A high reductant content is anticipated to yield a lower valence state of the resulting MnO_x (Wang et al., 2018). The fast transition from layer to tunnel necessitates a heightened reductant content (Ruiz-Garcia et al., 2021), even the main species of Mn maintained as Mn(IV) in the tunnel MnO_x (Yang et al., 2018). We speculate that other components instead of reductant contents could be dominant for the layer-to-tunnel transformation. Considering the Mn valence state in the tunnel MnO_x, the reoxidation of Mn(II)/Mn(III) to Mn(III)/Mn(IV) (Hu et al., 2019; Inoué et al., 2019) should be indispensable for the construction of tunnel MnO_x. Some studies highlighted the contribution of Mn(III) instead of Mn(II) to the tunnel MnO_x formation (Wang et al., 2019; Yang et al., 2018), and the generation and maintenance of Mn(III) on the MnO_x would need the participation of oxidants. In short, the cooperation of reductants and oxidants could be critical to determining the layer-to-tunnel transformation of MnO_x.

The oxidative conversion of Mn intermediates under the reduction conditions may necessitate intricate and specific cooperation of reducing and oxidizing components, a facet that is largely disregarded in prevailing research. The emergence of tunnel MnO_x is typically contingent on the antecedent formation of an inner complexed metal–MnO_x structure (Peacock & Moon, 2012; Ruiz-Garcia et al., 2021). In addition, locally combined Mn(III) on the MnO_x was reported to be vital for the tunnel MnO_x transformation as the launching step, and its formation required a sorption of Mn(II) and afterward electron transfer process (Mn(II) *vs.* Mn(IV)) (Yang et al., 2018). All these results underscore the importance of the local redox environment for the MnO_x transformation, which required a detailed assessment of the redox state at a sub-nanoscale level. An exhaustive appraisal of the electron transfer mechanisms during MnO_x transformation and the pivotal steps involving the collaboration of redox moieties is imperative for a comprehensive understanding of the fate of soil Mn and concomitant elements.

To assess the contribution of the redox components' cooperation on MnO_x transformation, pyrogenic carbon and trace elements (thallium) are selected as the representative soil components with MnO_x. Pyrogenic carbon (PC) is an ancient yet burgeoning form of soil organic matter distinguished by its pronounced redox reactivity, showing increasing importance in altering the fate of soil organic matter (Weng et al., 2022), redox-active minerals, and toxic metals (Xu et al., 2022b). Low-severity wildfires with incomplete biomass combustion (Bodí et al., 2014; Lopez et al., 2023) and the escalating application for soil conditioning and carbon sequestration (Lehmann, 2007; Lehmann et al., 2021) driven an annual soil carbon accumulation of 337 TgC yr^{-1} globally in the past years (Bowring et al., 2022). PC has rich surface functionality (Kluepfel et al., 2014; Xu et al., 2022b) with a defect-rich graphitic-like structure (Sun et al., 2017) that may provide substantial redox activities for soil minerals' transformation. These redox properties are intricately linked to the fundamental properties of PC and its formation conditions (Zhang et al., 2018; Zhang et al., 2019). For instance, the reduction of Fe minerals by PC commences with direct electron donation from carbon to Fe, further facilitated by the inherent valence change of Fe(II)/Fe(III), and low-temperature produced one showed a better reducing impact on the iron minerals (Xu et al., 2022b). The elucidation of redox-related MnO_x transformation with PC warrants attention, particularly in the context of mineral transformation pathways.

Thallium (Tl) is a highly toxic element classified as one of the priority pollutants by the European Water Framework and the U.S. Environmental Protection Agency, and it is listed in China's latest catalog of key metals for prevention (Liu et al., 2018; Liu et al., 2023). The long-term low-dose or acute high-dose exposure to thallium may cause gastrointestinal, neurological, and dermatological symptoms and even result in death (Wu et al., 2019a, 2019b; Peter & Viraraghavan, 2005). Tl exists as both Tl(I) and Tl(III) in soil, with the former being more toxic to various organisms and displaying higher mobility (Trainer et al., 2021). Anthropogenic sources, particularly metal mining and cement production, release an estimated annual quantity of 2000–5000 tons of Tl (Voegelin et al., 2015), leading to increasing attention in recent years (Liu et al., 2023). Tl-rich soil (up to over 100 mg kg^{-1}) has been reported in China (Du et al., 2024; Liu et al., 2018), Switzerland (Voegelin et al., 2015), Poland (Lis et al., 2003), and Mexico (Cruz-Hernández et al., 2018), strongly correlated with Mn minerals (Cruz-Hernández et al., 2018; Voegelin et al., 2015) through both oxidative and non-oxidative uptake (Wick et al., 2019). The redox reaction between Tl and MnO_x can be induced by the sorption of Tl on the vacancy sites of MnO_x and the subsequent formation of stable triple-corner sharing inner Tl complex structures (Manceau & Steinmann, 2023; Ruiz-Garcia et al., 2021) or Tl oxides (Cruz-Hernández et al., 2019). Both reduction and oxidation of Tl could occur with the MnO_x during the interaction (Cruz-Hernández et al., 2019; Peacock & Moon, 2012), leading to the large uncertainty of the Tl toxicity related to its redox state (Tl(I) or Tl(III)), induced MnO_x transformation, and affiliation with different MnO_x.

We hypothesize that the cooperation between reductants and oxidants may be key to transforming MnO_x from layered to tunnel structures. To explore this hypothesis, we evaluated the MnO_x transformation with different PCs and Tl, both capable of participating in either the reduction or oxidation. Poorly crystalline birnessite (layer-structured MnO_x), the most abundant natural MnO_x (Villalobos et al., 2003), was selected because it is a critical sink for the soil elements. Through a strategic combination of microcosm incubation, metal species evaluation, advanced microscopy (*e.g.,* spherical aberration-corrected transmission electron microscope (ACTEM)), and spectroscopy (*e.g.,* synchrotron X-ray absorption spectroscopy (XAS)), we first unveil the pivotal role of pairwise redox components to the layer-to-tunnel MnO_x transformation and shed light on the relevant geochemistry processes with trace elements.

2. Materials and methods

2.1. Production of birnessite and pyrogenic carbon

Birnessite was synthesized by reducing $KMnO_4$ with $MnCl_2$ following the reaction shown in **Eq.1** (Ruiz-Garcia et al., 2021). An excess amount of sodium hydroxide was mixed with $KMnO_4$ before the drop-addition of $MnCl_2$ solution. The addition was conducted with a 30-minute stirring, and the formed precipitates were further stirred for another 90 min before filtration. The collected solids, birnessite, were washed with DI water several times before freeze-drying and stored in a container with dry N_2 gas purging. X-ray diffraction (XRD) confirmed the formation of birnessite.

$$2KMnO_4 + 3MnCl_2 + 4NaOH + 4H_2O \rightarrow 5MnO_2 + 2KCl + 4NaCl + 6H_2O \quad (1)$$

Pyrogenic carbon (PC) was produced by the pyrolysis of woody yard waste in Hong Kong (obtained with the assistance of the Environmental Protection Department of the Hong Kong Government) under the N_2 atmosphere. The pyrolysis temperatures were selected as 400 and 700℃, representing the typical temperature range for the pyrogenic carbon reported in the literature, and they would show a contrasting redox performance (Kluepfel et al., 2014, Xu et al., 2020). The formed black solid carbon was collected and stored in the container under the N_2 atmosphere before further experiments. We refer to these two samples are PC400 and PC700 hereafter.

The electron-donating capacity (EDC) and electron-accepting capacity (EAC) of both PC400 and PC700 were quantified by the mediated electrochemical reduction (MER) and oxidation (MEO) methods (Kluepfel et al., 2014). Briefly, the working potential was set at 0.61 V, and ABTS (2, 2′-azino-bis (3-ethyl-benzthiazoline-6-sulfonic acid) diammonium salt) was selected as the mediator for the MEO reaction. For the MER test, Ziv (Zwitterionic viologen 4,4′-bipyridinium-1,1′-bis(2-ethylsulfonate)) was chosen as the mediator, and the working potential was set at −0.49 V. Both EDC and EAC were calculated based on integrating the current peak response with triplicates (Eq.1–2). Details can be found in Appendix S1.

$$EDC = \frac{\int \frac{I_{Ox}}{F} dt}{m_{PC}} \quad (1)$$

$$EAC = \frac{\int \frac{I_{Red}}{F} dt}{m_{PC}} \quad (2)$$

where I_{Red} and I_{Ox} [A] are the corrected electrochemical currents in the MER and MEO tests, respectively; F [s A (mol e^-)$^{-1}$] is the Faraday constant; and m_{PC} [g] is the mass of the pyrogenic carbon.

2.2. Incubation of birnessite with reductants and oxidants

Based on the typical concentrations of Mn minerals (~500 mg kg^{-1}), PC (~500 mg kg^{-1}), and Tl (up to 3.16 mg kg^{-1}) (Jiang et al., 2022) in the soil, 0.5 g PC and 0.5 g birnessite were mixed in 200 mL Tl-containing solution (~2.6 mg Tl(III) in the forms of $Tl(NO_3)_3$ or Tl(I) in the forms of $TlNO_3$). PC and Tl can serve as reductants and oxidants, respectively, to trigger the transformation of birnessite. Incubation of birnessite with only PC or Tl was set in parallel to further evaluate the contribution of pairwise existing redox components. All incubation settings were conducted in triplicate. The pH was controlled at ~ 6.5–7.0 by diluted HCl or NaOH, and it was maintained at 6.5–7.6 during the whole incubation, similar to the soil conditions (Appendix 21). The incubation was conducted for 16 weeks, and the solid samples were collected at the selected time intervals (weeks 1, 2, 4, 6, 8, 12, and 16) to evaluate the solid-phase transformation. Notably, to exclude the impact of O_2 and the generated radicals as the oxidant during the incubation process, 30 mins N_2 gas purging was conducted on all deionized (DI) water with heating before the utilization.

2.3. Soil incubation and sampling

Soil incubation experiments were conducted in paddy soil collected from Jiangsu Provine, China, classified as silt loam (IUSS Working Group, 2014) (6.34 % sand, 79.2 % silt, and 14.4 % loam). The selected soil has a limited Fe/Mn content (11.6 g kg^{-1} for Fe and 0.1 g kg^{-1} for Mn) with a neutral pH value (7.5), minimizing its potential effect on the subsequent study of the birnessite transformation. Binessite (500 mg kg^{-1}) and PC (500 mg kg^{-1}) were added to the soil, and the moisture content was to be 20 wt% by adding DI water. Tl concentration in the soil was controlled as ~ 2.6 mg kg^{-1} by spiking the Tl solution in either oxidative Tl(III) forms ($Tl(NO_3)_3$) or reductive Tl(I) ($TlNO_3$) as control, representing the typical Tl contamination in the paddy soil (up to 3.16 mg kg^{-1}) (Jiang et al., 2022). The control groups without birnessite, Tl, or pyrogenic carbon were set in parallel. The incubation lasted for 16 weeks, and the water content was controlled by replenishing DI water weekly. The soil samples were collected at week 4, week 8, and week 16, air-dried, crushed, and stored at −4℃ before further characterization, and triplicates were conducted for each setting.

2.4. Mn Transformation analysis

XRD analysis was first conducted to evaluate the crystal structure transformation of the MnO_x during the 16-week incubation period. ACTEM combined with Energy Dispersive X-ray spectroscopy (EDX), Electron Energy Loss Spectroscopy (EELS), and Selected Area Electron Diffraction (SAED) analysis were used to characterize the particle morphological and association information of Mn, Tl, and C. X-ray photoelectron spectroscopy (XPS) analysis with depth profiling was conducted to evidence the valence transformation and the depth distribution of the key elements. Moreover, Mn K-edge XAS analysis was conducted to unveil the local coordination environment of Mn during the incubation process. Details for the XAS data collection and analysis can be found in Appendix S3.

2.5. Tl speciation analysis

The fate and stability of Tl were first evaluated by the different extraction analyses, including $CaCl_2$, CH_3COONH_4 (Wick et al., 2020), $(NH_4)_2C_2O_4$ (Voegelin et al., 2015), and $NH_2OH{\cdot}HCl$ (Marafatto et al., 2021) extraction. $CaCl_2$ extraction mainly targets the surface-sorbed Tl, which can be replaced with Ca, and CH_3COONH_4 can extract the Tl on the surface and within the mineral layer due to its lower hydrated radius (Wick et al., 2020). Both $(NH_4)_2C_2O_4$ and $NH_2OH{\cdot}HCl$ can dissolve the MnO_x to different extents based on the reduction and chelation process, and they can extract Tl, which is incorporated into the MnO_x. The extracted/dissolved content of Mn during each extraction method was quantified. Details for these extraction procedures are summarized in Appendix S4.

In addition, Tl L_3-edge XAS data was collected to characterize the Tl local structure during the MnO_x transformation process. The valence state of Tl under the different layers of the MnO_x was determined by XPS analysis, and its distribution in the MnO_x was visualized by the ACTEM. The leachability of Tl was evaluated by extraction using soil organic acids derived from root exudates, microbial secretion, and plant decomposition (Xu et al., 2019). The bioaccessibility of Tl during the incubation with MnO_x and PC was evaluated using the in vitro physiologically based extraction test (PBET) in the gastric phase that was simulated with organic acids and pepsin (Ruby et al., 1996). Details for selecting soil organic acids and PBET are elaborated in Appendix S5. Inductively coupled plasma-optical emission spectrometry (ICP-OES) or mass spectrometry (ICP-MS) was used to detect the Tl concentrations after the acidification and solid digestion.

3. Results

3.1. MnO_x transformation

The pristine MnO_x showed a typical crystal structure of birnessite (Fig. 1), generally denoted as a layered 2 × ∞ structure with the basic unit as the Mn–O octahedron. The formation of hollandite, a tunnel MnO_x with a 2 × 2 structure, was found after 6-week incubation with Tl (III) and PC400, and its crystallinity continued to grow during the 16-week incubation (Fig. 1**a**). A slower layer-to-tunnel transformation occurred with the Tl(III) and PC700, with minor peaks emerging after more than 12 weeks of incubation (Fig. 1**b**). Unlike Tl(III), the incubation with Tl(I) showed limited impact on inducing the MnO_x transformation with either PC400 or PC700 (Fig. 1**d & 1e**). No tunnel structures were formed during the 16 weeks of incubation with Tl alone (Fig. 1**c & 1f**). Peaks of tunnel MnO_x occurred after 12 weeks of

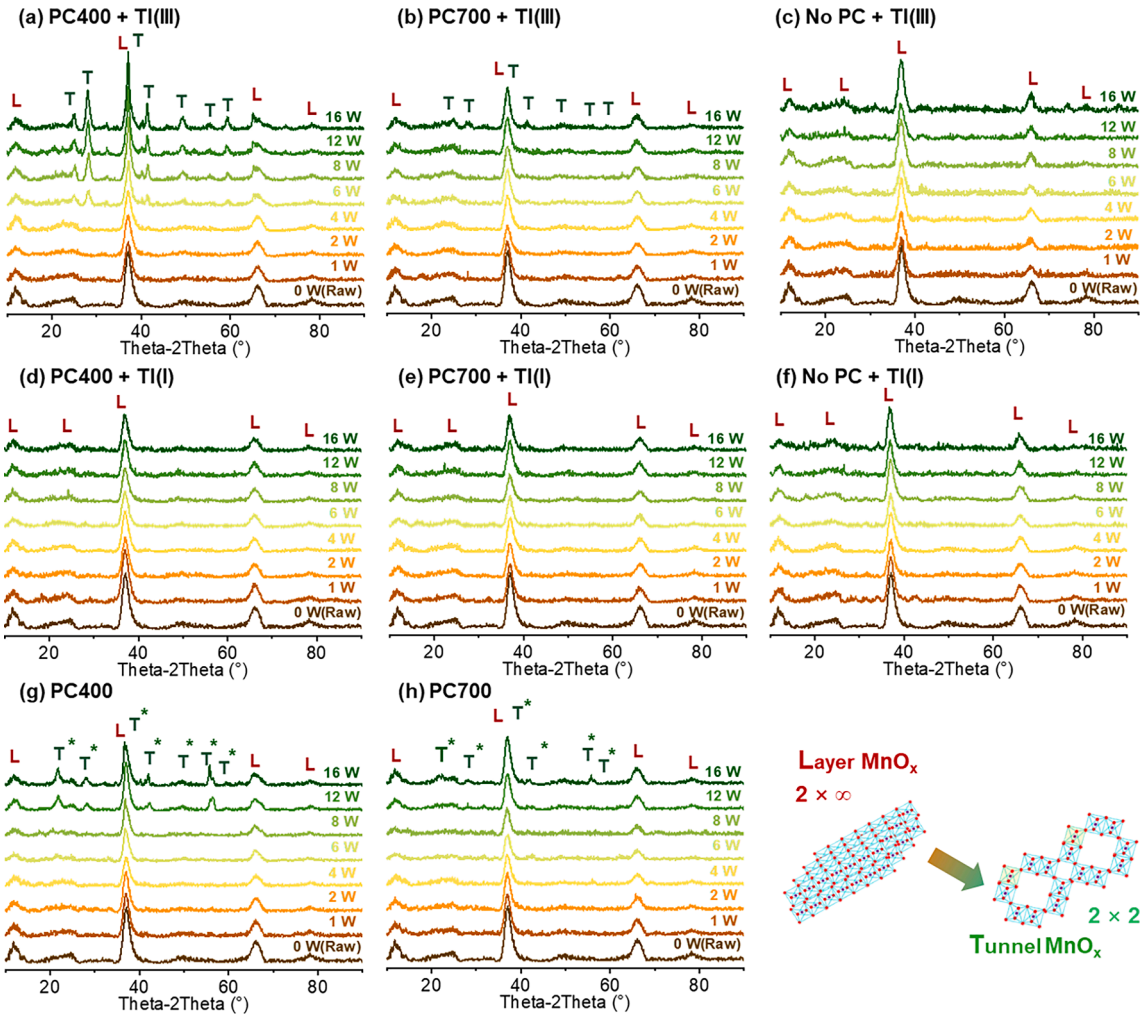

Fig. 1. XRD patterns of MnO_x incubated with different pyrogenic carbon (PC400 or PC700) and Tl (L: Layer-structured MnO_x with 2×∞ structure, birnessite; T: Tunnel-structured MnO_x with 2 × 2 structure, hollandite; T*: Tunnel-structure MnO_x with 1 × 1 or 1 × 2 structure). 0 W represents the raw birnessite without incubation. Formation of tunnel-structured MnO_x occurred after 6 weeks of incubation with PC400 and Tl(III), while limited layer-to-tunnel transformation was found with PC700 or Tl(I).

incubation with PC alone, which belong to the MnO_x with 1 × 2 or 1 × 1 structure and high disorder degree (Fig. 1**g & 1h**).

3.2. Mn stability during transformation

Extraction analysis was conducted to evaluate the transformation of MnO_x with Tl and PC (Appendix S4 & Appendix S6). Approximately 90 % of Mn can be extracted by $NH_2OH{\cdot}HCl$ due to its strong reduction capacity and high acidity, while a relatively lower content of Mn can be extracted by $(NH_4)_2C_2O_4$ (with lower reducing capacity). The varying extraction amounts may indicate the different stability of the MnO_x during incubation with PC and Tl. Furthermore, we computed the variance between the two extraction methods, which may denote the MnO_x with relatively high stability, as it can only be extracted by strong $NH_2OH{\cdot}HCl$, while the remaining portion pertains to the low-stability MnO_x (Fig. 2**a**).

The low-stability MnO_x decreased from 73.7 % to 49.7 % during the 16-week incubation with PC400 and Tl(III), while a smaller decrease was observed with PC700 and Tl(III) (73.7 % to 62.0 %) (Fig. 2**a**). The Tl (I) incubation systems showed less variation in MnO_x stability with either PC400 or PC700 (from 73.7 % to 66.9–71.4 % during the 16-week incubation). For the incubation without PC, an increase in the low-stability MnO_x was observed, and Tl(I) induced a more apparent increase to 89.1 % compared to Tl(III) (83.1 %).

3.3. Fate of Tl during transformation

Based on the complete dissolution of $NH_2OH{\cdot}HCl$ on MnO_x, over 90 % Tl can be extracted, and the proportion remained unchanged during the incubation process (Appendix S6). The partial dissolution of the MnO_x by $(NH_4)_2C_2O_4$ led to a relatively lower release amount of Tl, and its content changed with the incubation process. Based on the extraction results, Tl predominantly existed in the crystal structure of the MnO_x (over 88 % of Tl extracted by the MnO_x dissolution, *i.e.,* $NH_2OH{\cdot}HCl$ or $(NH_4)_2C_2O_4$ extraction), and the extraction amount of Tl varied during the incubation (Fig. 2**b** and Appendix S6). In the presence of Tl(III) and PC400, the percentage of Tl combined with low-stability Mn (extracted by $(NH_4)_2C_2O_4$) decreased from 55.9 % (week 1) to 12.8 % (week 16), while the percentage of Tl combined with high-stability Mn (extracted by $NH_2OH{\cdot}HCl$) concurrently increased to 75.2 % (week 16) (Fig. 2**b**). PC700 with Tl(III) only induced a slighter decrease of Tl combined with low-stability Mn from 56.4 % (week 1) to 40.7 % (week 16), and Tl(III) alone can only cause a decrease from 65.3 % (week 1) to 50.7 % (week 16) (Fig. 2**b**). A much more neglectable decrease was found in the Tl(I) system (Fig. 2**b**). Incubation with Tl(I) and PC only caused a decrease of the Tl combined with low-stability Mn from 35.8–37.6 % (week 1) to 26.1–31.0 % (week 16), with a slight increase of Tl combined with high-stability Mn from 56.4–57.6 % (week 1) to 61.0–64.8 % (week 16). Tl(I) alone induced a more apparent transformation than PC, and Tl

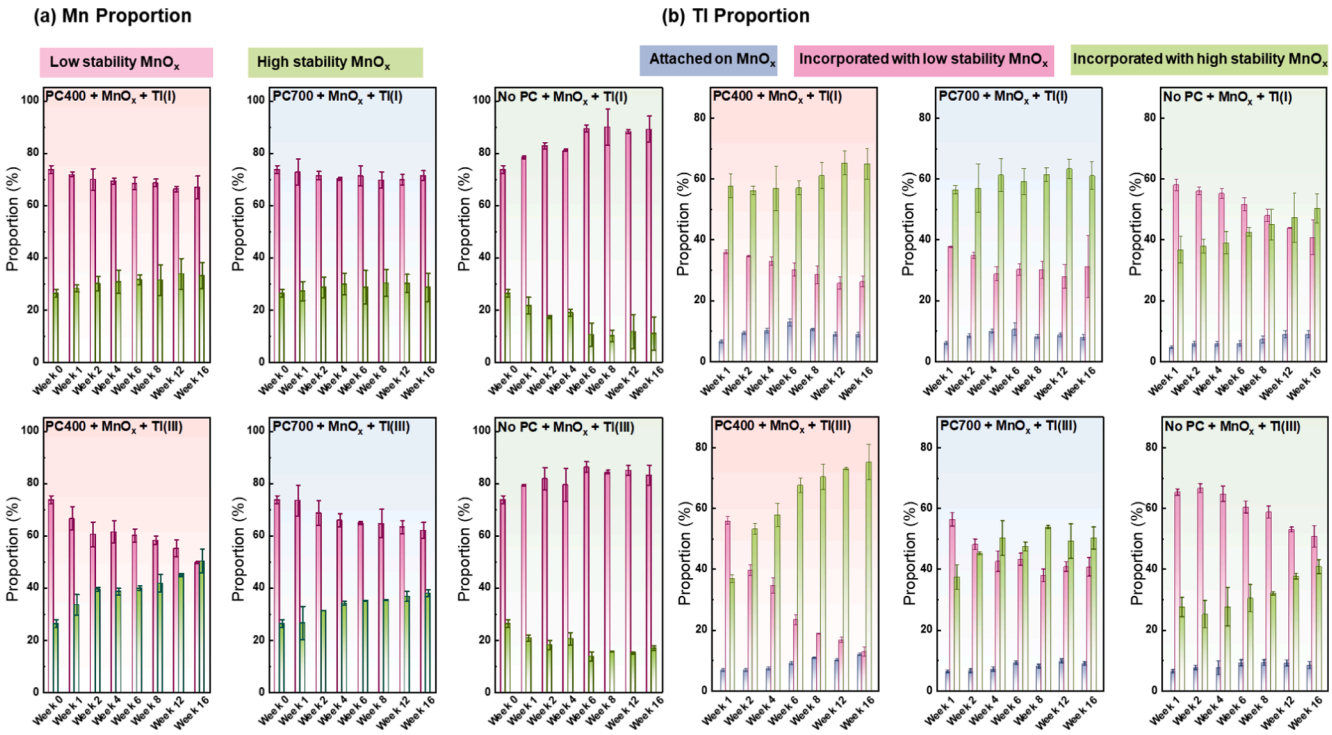

Fig. 2. The change of Mn (a) and Tl (b) proportions during the incubation with PC and/or Tl. Low-stability MnO_x was calculated based on the extraction amount by $(NH_4)_2C_2O_4$, while the difference between Mn content extracted by $(NH_4)_2C_2O_4$ and $NH_2OH{\cdot}HCl$ was denoted as the high-stability MnO_x. A significant increase in the high stability of MnO_x occurred with PC400 and Tl(III) during incubation. The Tl attached to the MnO_x was calculated based on the extraction amount of Mn through CH_3COONH_4. The difference between CH_3COONH_4 and $(NH_4)_2C_2O_4$ (low-stability MnO_x) or $(NH_4)_2C_2O_4$ and $NH_2OH{\cdot}HCl$ (high-stability MnO_x) was used to determine the Tl incorporated within the MnOx. Notably, a limited soluble Tl and surface-attached Tl on MnO_x (extracted by $CaCl_2$) was detected (see Appendix S6). Week 0 represents the birnessite without incubation.

combined with low-stability Mn decreased from 58.0 % (week 1) to 40.6 % (week 16).

In addition to the Tl that existed in the crystal structure of MnO_x, a substantial proportion of Tl was attached in the interlayer of MnO_x (4.2–12.0 %, extracted by CH_3COONH_4), and a relatively lower amount was attached on the surface (0.3–1.2 %, extracted by $CaCl_2$) (Fig. 2**b** and Appendix S6). We compared the change of Tl attached on the MnOx (sum of the surface attached amount and interlayer attached amount) (Fig. 2**b**). During the incubation with PC and Tl(III), the attached Tl increased from 6.2–6.8 % to 8.3–11.9 %. For the Tl(I) system, a fast rise of the attached Tl occurred within the first six weeks of incubation (from 5.9–6.4 % to 10.4–12.7 %), while a sustainable decrease to 7.8–8.7 % was shown during the subsequent incubation with PC.

3.4. Tl and Mn turnover in soil

A similar phenomenon of Tl/Mn turnover was observed in the soil incubation systems. During the incubation with Tl(III), a discernible decrease of Tl associated with low-stability Mn (extracted by $(NH_4)_2C_2O_4$ only) was evident throughout the entire incubation period compared to the group without PC (Fig. 3). PC400 triggered the decrease of Tl associated with low-stability Mn from 1.11 mg kg^{-1} to 0.53 mg kg^{-1}, while a less decrease was found with PC700 (from 1.11 mg kg^{-1} to 0.74 mg kg^{-1}) (Fig. 3**a**). In addition to the Tl within the crystal structure of MnO_x, the surface-attached Tl and interlayer fixed Tl showed a sustainable decrease with PC, especially with PC400. The extracted Mn by $(NH_4)_2C_2O_4$ decreased from 352.5 mg kg^{-1} to 243.9 mg kg^{-1} and 289.2 mg kg^{-1} with PC400 and PC700, respectively, and both were lower than that in the control group (357.5 mg kg^{-1}) (Fig. 3**b**). Less variation of both low-stability Tl (from 1.07 mg kg^{-1} to 0.83 mg kg^{-1}) and Mn (from 370.2 mg kg^{-1} to 301.2 mg kg^{-1}) was observed when selecting Tl(I) as the Tl source (Appendix S7).

3.5. Tl bioaccessibility and leachability

In the Tl(III) system, PC400 could effectively reduce the bioaccessibility of Tl after 4 weeks of incubation compared to the control group without PC (15.2 % < 38.9 %, Fig. 3**c**), and a further decrease was found with prolonged incubation (8.7–8.9 %). A lower impact was found with PC700 during the incubation process (24.4–26.7 %). Limited impact was found in the Tl(I) system for either PC400 (25.4–31.5 %) or PC700 (29.0–29.3 %), with a slightly lower bioaccessibility in the control group without PC (33.7–36.5 %) (Appendix S7).

The leachability of Tl in soil with different soil organic acids (Appendix S5) signifies the enhanced stability of Tl and Mn during the layer-to-tunnel transformation (Fig. 3**d**). Four typical soil organic acids were used to extract the Tl, and a lower proportion of Tl can be extracted with PC400 (0.05–0.26 mg kg^{-1}) compared to PC700 (0.08–0.41 mg kg^{-1}) by all organic acids in the Tl(III) system. Oxalic acid (0.18–0.41 mg kg^{-1}) and tartaric acid (0.13–0.32 mg kg^{-1}) showed an apparent higher impact on the Tl leaching compared to the malic acid (0.12–0.24 mg kg^{-1}) and succinic acids (0.05–0.09 mg kg^{-1}). Notably, limited variation of the extracted Tl amount occurred when selecting Tl(I) as the Tl source for the soil incubation (Appendix S7). Approximately 0.15–0.45 mg kg^{-1} could be extracted by different organic acids after 4 weeks of incubation with Tl(I) and PC, the extraction amount maintained after 16 weeks of incubation (0.15–0.44 mg kg^{-1}) (Appendix S7). The leachability of Tl with PC was similar to that without PC (0.18–0.50 mg kg^{-1}) in the Tl(I) system during the whole incubation process.

3.6. Morphology evaluation

TEM-EDX analysis confirmed the MnO_x transformation during the interaction with PC 400 and Tl(III) (Fig. 4**a**). MnO_x transformed from an amorphous phase (layer MnO_x birnessite, 1–4 weeks) to a crystal needle-

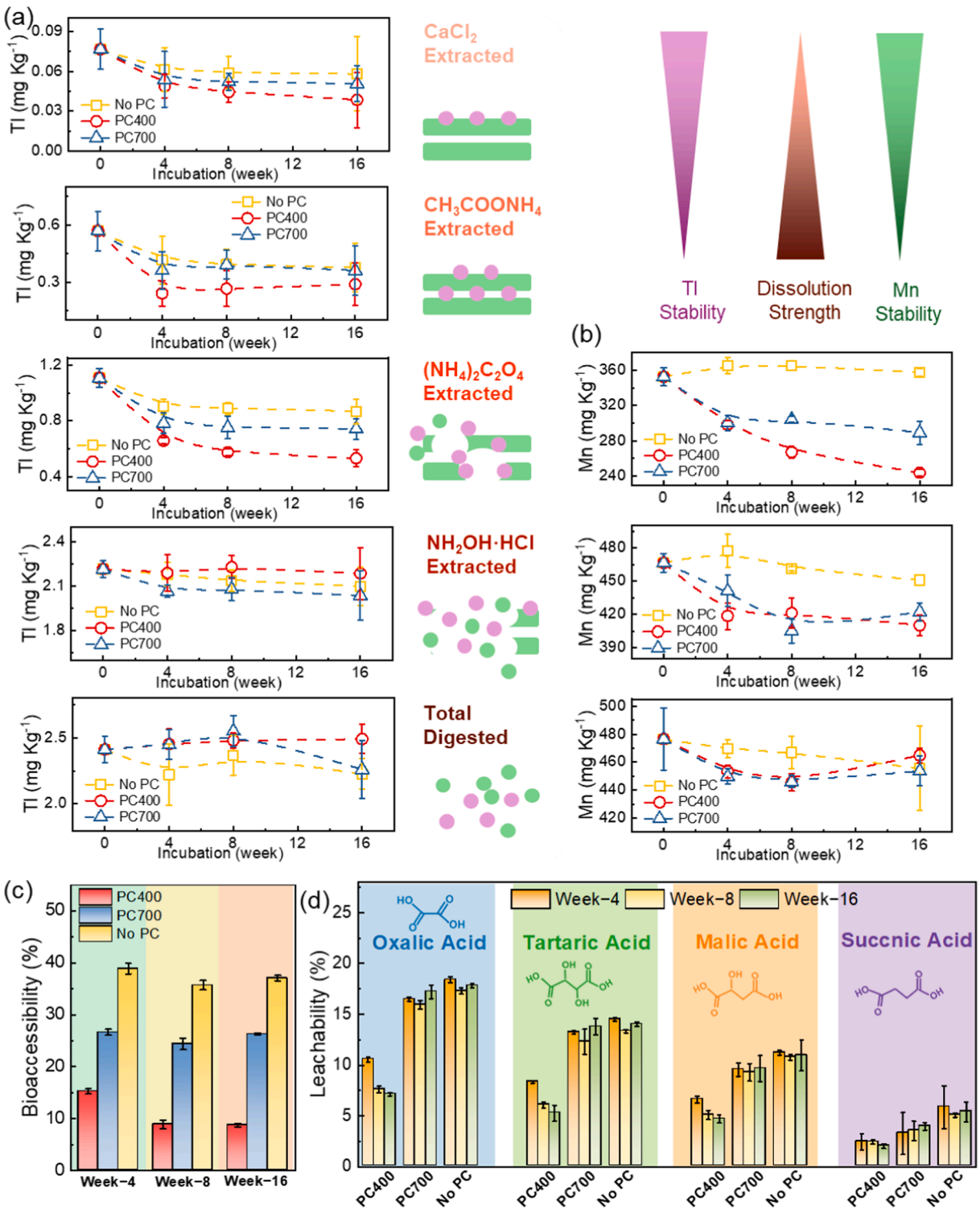

Fig. 3. The extraction amount of Tl (a) and Mn (b) from the soil incubated with Tl(III), PC, and MnO_x with different extraction approaches; Bioaccessibility (c) and leachability of Tl by different soil organic acids (d) from the soil incubated with Tl(III), PC, and MnO_x.

like structure (tunnel MnO_x, hollandite, 8–16 weeks) during the incubation process, consistent with the XRD findings. The tunnel-like structure started to appear after four weeks of incubation, and its crystallinity continued to increase during further incubation based on the SAED patterns (Appendix S8). Similarly, less transformation of Mn minerals occurred in the Tl(I) incubation system based on the morphology analysis (Appendix S9). TEM-EDX analysis showed a high correlation of Tl and Mn in both layer and tunnel MnO_x (Fig. 4**a**), evidencing the fixation of Tl on Mn minerals with different speciation.

ACTEM-High-Angle-Annular-Dark-Field (HAADF) analysis was then conducted to reveal the distribution of Tl during the incubation. Due to the disparity in the atomic weight, Tl appeared as brighter spots in the HAADF version, which can visualize the incorporation of Tl during the incubation process with PC. Tl was mainly attached to the MnO_x surface during the first 4 weeks of incubation (Fig. 4**b**). Along with the layer-to-tunnel transformation (week 4–week 8), Tl (van der Waals radius as

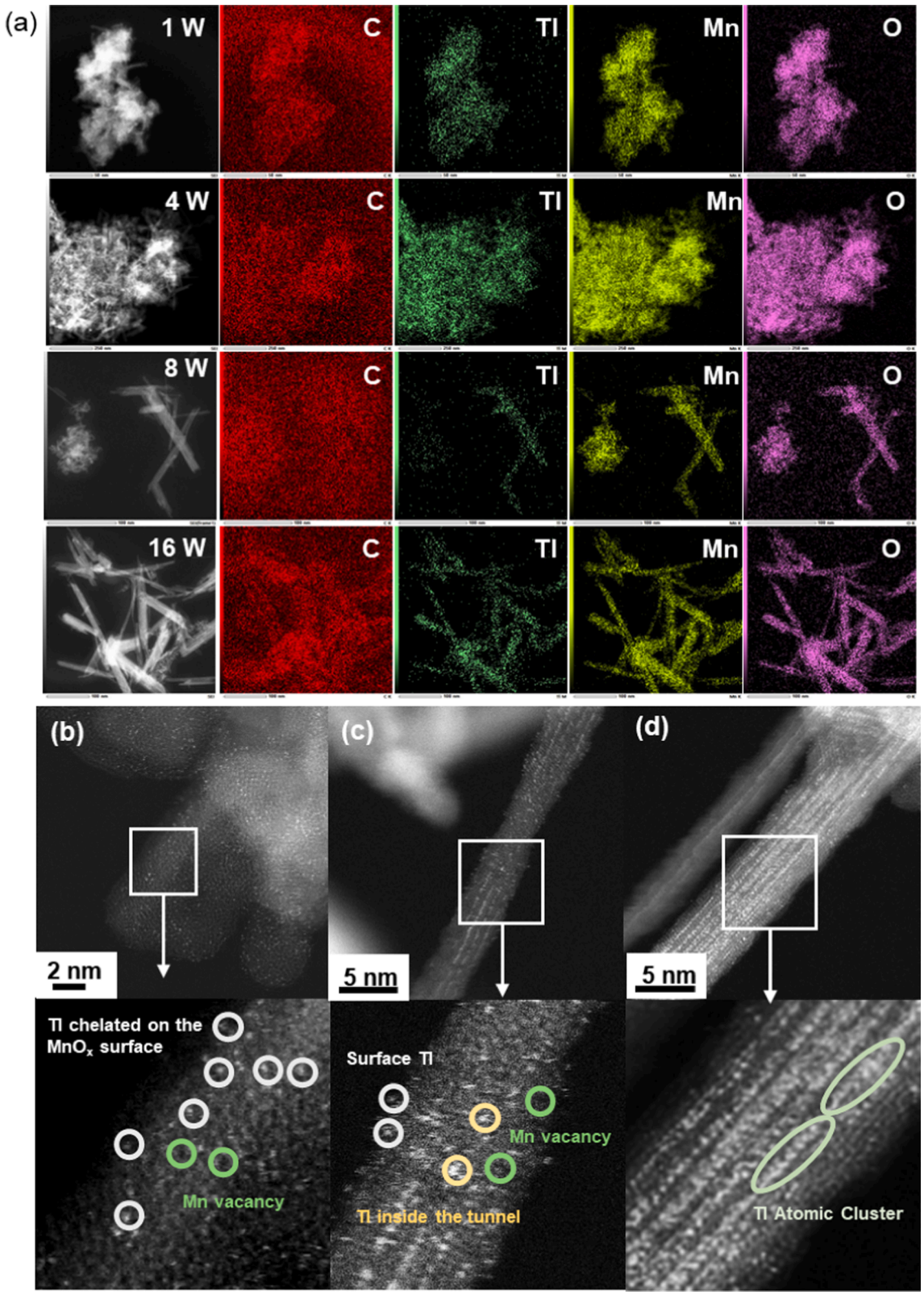

Fig. 4. TEM-EDX images of MnO_x after incubation with PC400 and Tl(III) (a); ACTEM-HAADF images of MnO_x after 4 weeks (b), 8 weeks (c), and 16 weeks (d) of incubation with Tl(III) and PC400. The enlarged version below shows the distribution of Tl and Mn vacancies. ACTEM-HAADF analysis revealed the Tl incorporation in the tunnel MnOx, Mn vacancy formation, and Tl aggregation during the whole incubation process.

2.60 Å) was embedded inside the tunnel structure of MnO_x (2 × 2 with diameter = ~4.6 Å (Yuan et al., 2024)) and distributed as single Tl atoms (Fig. 4**c**). With prolonged incubation, a continuous accumulation of Tl inside the tunnel can be observed (Fig. 4**d**), implying the preference for Tl to be fixed on the high-stability MnO_x. Due to the increasing numbers of Tl atoms in the tunnel MnO_x along with the incubation process, Tl atoms tended to form an atomic cluster after 16 weeks of incubation (Fig. 4**d**). Notably, the high-resolution image of the ACTEM indicated the existence of the Mn vacancies on the MnOx, which can be shown as the black deficiency in the crystal structure. Mn vacancies can be widely found in the MnO_x after 4–8 weeks of incubation (Fig. 4**b** & **4c**), while a well-growth crystal lattice was shown in the MnO_x after 16 weeks of incubation (Fig. 4**d**).

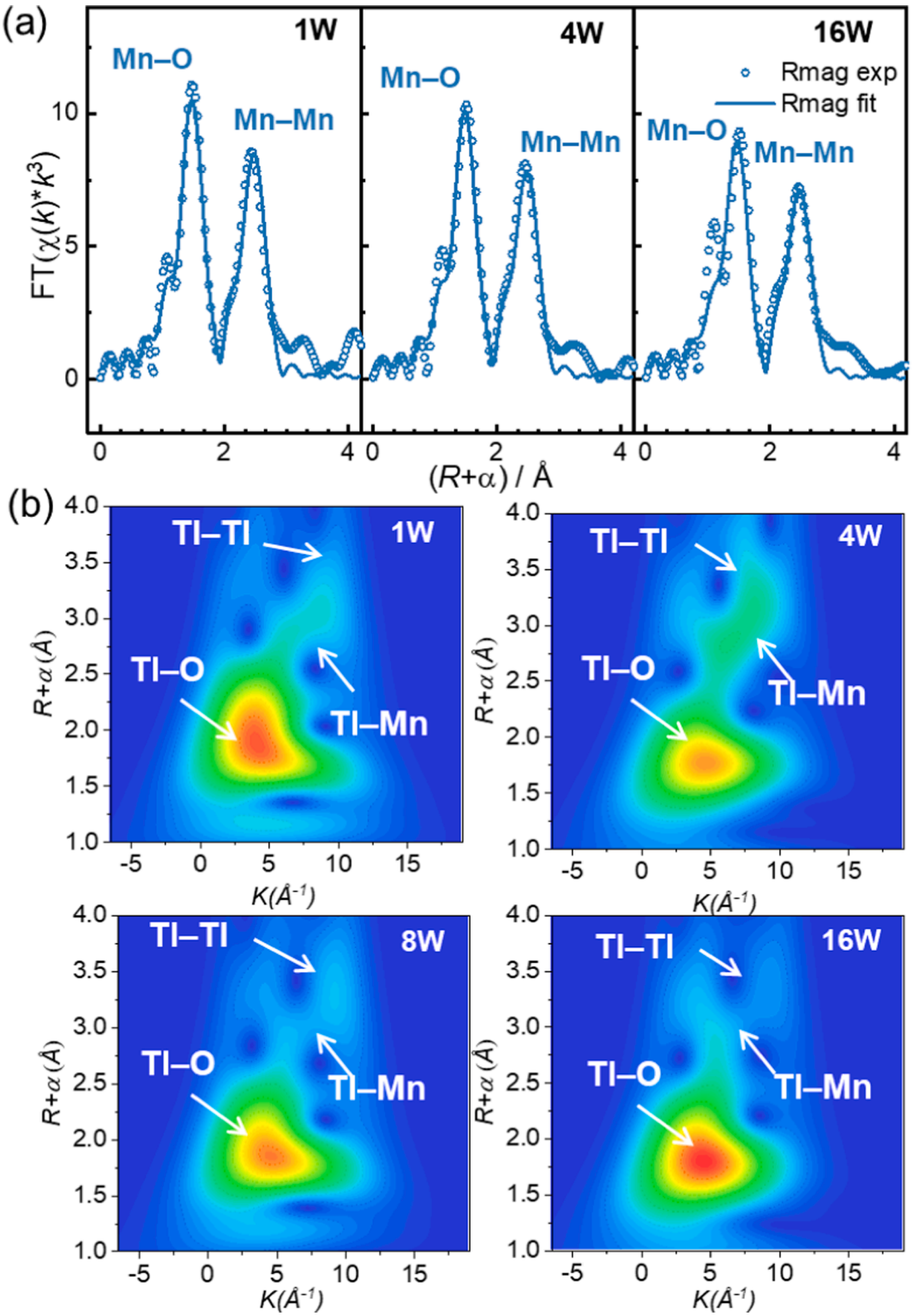

Fig. 5. Mn K-edge EXAFS spectra in R + ΔR-space of MnO_x after incubation with PC400 and Tl(III) (a). The fitting output (solid lines) is overlain with the data (dotted lines). WT-EXAFS of Tl L3-edge in the MnO_x during the incubation with PC400 and Tl(III) (b).

3.7. Local coordination environment of Mn

Shell-by-shell fitting of extended X-ray absorption fine structure (EXAFS) data was conducted to evaluate the local coordination environment of Mn minerals during the incubation process. Due to the stable structure of the basic Mn–O octahedron, no significant difference in the Mn–O path could be found during the incubation process, especially for the path radius (1.89 Å) (Fig. 5 and Appendix S3). A slight increase in the coordination number was found throughout the incubation process, probably indicating the crystallization of the mineral structures with a longer incubation time. It is worth noting that the coordination number of Mn–O was approximately 4.4–4.5, which was less than 6 in the standard octahedron, and it indicated the formation of O vacancy with less Mn valence state on the MnO_x samples during the whole incubation. The radius of the Mn–Mn path increased from 2.90 Å (1 week) to 2.94 Å (16 weeks) during the incubation of birnessite with Tl(III) and PC400 (Fig. 5 and Appendix S3), and the coordination number of the Mn–Mn path increased from 4.8 to 5.1. Notably, a limited extent of transformation of the Mn–Mn path could be found after 16 weeks of incubation with PC400 and Tl(I), again evidencing the less transformation of the MnO_x with Tl(I) (Appendix S3).

3.8. Local coordination environment of Tl

The chemical information of the Tl attached to the Mn minerals was evaluated during the 16 weeks of incubation (Table 2, Fig. 5**b**, and Appendix S3). In addition to the typical Tl–O1 path in the Tl-attached Mn mineral samples (R = ~2.28 Å) (Wick et al., 2019), another Tl–O2 path with a relatively long interatomic distance was found in all the samples (R = 2.42–2.45 Å), which belong to the Tl–O in the Tl (hydr) oxides precipitated on the MnO_2 surface. Meanwhile, two Tl–Mn paths (R = 3.33–3.49 Å or 3.53–3.74 Å) and one Tl–Tl path (3.82–4.05 Å) can be detected in the second shell (Fig. 5**b**), which represents the typical coordinate structure in the Tl-sorbed MnO_x and Tl oxides (Cruz-Hernández et al., 2019; Wick et al., 2019).

With the first 4-week incubation, the coordination number of Tl–O2 and Tl–Tl decreased from 1.8 to 1.0 and from 3.3 to 2.5, respectively (Table 2), with the increase in coordination number of Tl–Mn path from 2.2 to 2.5 to 3.4–3.8. With the prolonged incubation of 8 weeks, the coordination number of Tl–O2, and Tl–Tl was reduced to 0.9 and 1.3, respectively. The coordination number of Tl–Mn decreased to 0.9–1.1, in contrast to the transformation in the first 4 weeks (Table 2), and the path radium of Tl–Mn decreased to 3.45–3.58 Å. With further incubation to 16 weeks, all paths showed increased coordination numbers compared to that after 8-week incubation. Notably, a shorter radius of either the Tl–Tl path (R = 3.82 Å) or Tl–Mn (R = 3.33–3.53 Å) was found along with the incubation process (Table 2).

Table 1
Shell-by-shell fitting results of Mn K-edge EXAFS data.

	Path	R Å	CN	σ^2	ΔE_0 (eV)	R-factor
Tl(III)-PC400-1w	Mn–O	1.89 (1)	4.4 (4)	0.003 (1)	−7.15	0.029
	Mn–Mn	2.90 (0)	4.8 (2)	0.006 (1)		
Tl(III)-PC400-4w	Mn–O	1.89 (1)	4.4 (3)	0.003 (1)	−6.86	0.034
	Mn–Mn	2.91 (1)	5.1 (3)	0.008 (2)		
Tl(III)-PC400-16w	Mn–O	1.89 (1)	4.5 (3)	0.005 (2)	−6.52	0.044
	Mn–Mn	2.94 (0)	5.1 (2)	0.009 (3)		
Tl(I)-PC400-16w	Mn–O	1.89 (1)	4.4 (3)	0.002 (1)	−3.29	0.024
	Mn–Mn	2.89 (1)	4.6 (4)	0.008 (2)		

Fitting parameters include CN, coordination number, R, interatomic distance, σ^2, squared Debye-Waller factor, ΔE_0, energy difference accounting for the phase shift between the overall experimental spectrum and FEFF calculation. Fitting quality was estimated using the R-factor. The passive electron reduction factor, S_0^2, was fixed at 0.85.

Table 2
Shell-by-shell fitting results of Tl L3-edge EXAFS data.

	Path[a]	R Å	CN	σ^2	R-factor
1w	Tl–O1	2.28(0)	2.2(1)	0.003(0)	0.006
	Tl–O2	2.42(0)	1.8(1)	0.000(0)	
	Tl–Mn1	3.49(0)	2.5(3)	0.014(1)	
	Tl–Mn2[a]	3.74(0)	2.2(4)	0.014(1)	
	Tl–Tl	4.05(1)	3.3(9)	0.029(9)	
4w	Tl–O1	2.28(0)	2.4(2)	0.005(0)	0.008
	Tl–O2	2.44(0)	1.0(2)	0.001(0)	
	Tl–Mn1	3.49(0)	3.8(8)	0.014(2)	
	Tl–Mn2	3.74(0)	3.4(8)	0.014(2)	
	Tl–Tl	3.93(0)	2.5(5)	0.011(0)	
8w	Tl–O1	2.29(0)	1.8(2)	0.002(1)	0.008
	Tl–O2	2.47(0)	0.9(2)	0.000(0)	
	Tl–Mn1	3.45(0)	0.9(4)	0.017(0)	
	Tl–Mn2	3.58(0)	1.1(4)	0.017(0)	
	Tl–Tl	3.84(0)	1.3(5)	0.006(4)	
16w	Tl–O1	2.28(0)	2.0(2)	0.004(1)	0.013
	Tl–O2	2.45(0)	1.2(2)	0.001(0)	
	Tl–Mn1	3.33(0)	1.4(4)	0.010(5)	
	Tl–Mn2	3.53(0)	2.0(7)	0.010(5)	
	Tl–Tl	3.82(0)	1.7(4)	0.007(4)	

Fitting parameters include N, coordination number, R, interatomic distance, and σ^2, squared Debye-Waller factor. Fit quality was estimated using the R-factor. The passive electron reduction factor, S_0^2, was fixed at 0.85.
[a] σ^2 of Tl-Mn1 and Tl-Mn2 was set as the same value during the fitting process.

3.9. Valence State of Tl/Mn

The valence state of Tl/Mn on different layers of MnO_x incubated with Tl(III) and PC400 was evaluated by XPS analysis with different etching times (*i.e.,* 0 s, 20 s, 40 s, 80 s, and 200 s) (Appendix S10). Basically, the Mn valence state in the surface 5 nm decreased from 3.60 to 3.10 during the incubation process, while its value in the inner 5–50 nm area increased from 2.42 to 2.91 to 2.42–3.06 (Fig. 6**a**). Meanwhile, the reductive transformation of Tl(III) to Tl(I) was nearly completed during the first 4 weeks of incubation, and Tl(III) remained at a low value of less than 10 % during the afterward incubation (Fig. 6**b**). Synchrotron-based X-ray Absorption Spectrum (XAS) analysis confirmed the reduction of Tl(III) with the generation of Tl(I) during the 16 weeks of incubation (Fig. 6**c**). Notably, the low valence state of Mn on the MnO_x implied the formation of O vacancy in the Mn–O octahedron (Appendix S3).

The reductive transformation of Mn mainly occurred in the deeper layer of the MnO_x during the incubation with Tl(III), while surface oxidation with a higher Mn valence state was found with PC700 or without PC (Fig. 6**d**). In the Tl(I) system, Mn showed a contrasting transformation both on the surface and inside of the MnO_x, *i.e.,* a decrease of Mn valence state on the surface with the increase of Mn valence state inside MnO_x. Tl(I) was the main species (>80 %) on the whole MnO_x in all incubation systems instead of that with Tl(III) alone (Fig. 6**e**). Over 90 % of Tl was Tl(III) on MnO_x after 4 weeks of incubation with Tl(III) alone, and it decreased to 40.0–62.0 % after 16 weeks of incubation.

4. Discussion

4.1. layer-to-tunnel transformation of MnO_x and its impact on the fate of Tl

The layer-to-tunnel transformation occurred during the incubation

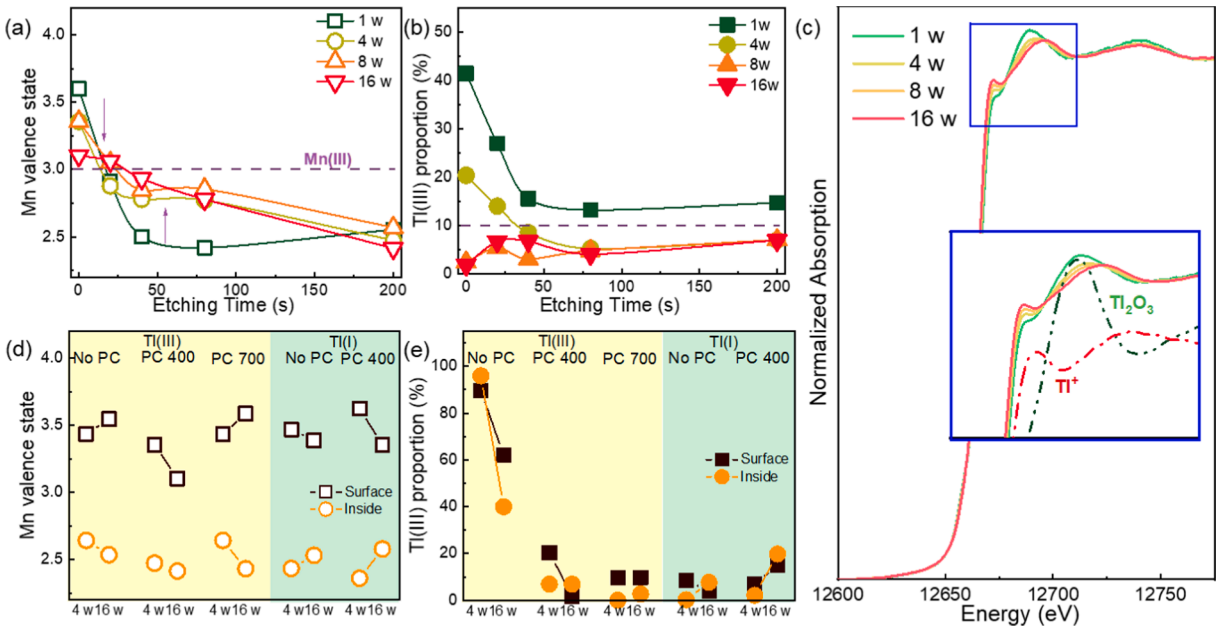

Fig. 6. Mn average valence state (a) and Tl(III) proportion (b) during the incubation of MnO_x with PC400 and Tl(III). Information under different depths was obtained by etching with a sputter rate of 0.25 nm/s for Ta_2O_5. Tl L3-edge XANES spectra of the sample during the 16 weeks of incubation (c) and the reference spectra of Tl^+ and Tl_2O_3 (dash line) were obtained from the reference (Wick et al., 2019). Mn average valence state (d) and Tl(III) proportion (e) during the incubation of MnO_x with different PC and/or Tl. The surface data was obtained from direct XPS analysis, while inside data was obtained after 200 s etching.

with Tl(III) and PC, especially with the PC400, evidenced by the XRD (Fig. 1) and TEM analysis (Fig. 4). The extraction experiment indicated that the formation of crystal tunnel MnO_x would increase its stability to resist the dissolution from soil organic acids and strong reductants such as $NH_2OH{\cdot}HCl$, thus reducing the mobility and bioaccessibility of the incorporated Tl. Therefore, a lower content of Tl can be extracted with PBET and soil organic acids after incubation with MnO_x and PC400 (Fig. 3). The potent combination of Tl with tunnel MnO_x indicated its lower threat to human health through the water system, and the limited extraction by root-derived organic acids suggested less possibility of biomagnification through the food chain (Liu et al., 2019). Moreover, the low extraction amount through PBET implied its low bioaccessibility and ingestion risk when incorporated into the tunnel MnO_x.

The combined spectroscopy and morphology analysis revealed the underlying mechanisms for the Tl turnover with the MnO_x (Fig. 7). At the beginning of the incubation (Week 0–4), accumulation of Tl on MnO_x with weak Tl–O–Mn bonding or existing as amorphous Tl oxides was the primary process with limited MnO_x transformation. The increasing Tl–Mn path, as evidenced by the EXAFS (Table 2), can be direct evidence for this process. Meanwhile, the increased proportion of interlayer-attached Tl on MnO_x in the first four weeks supports the accumulation of Tl (Fig. 2 and Appendix S6). The accumulation of the Tl was accompanied by the redox reaction of Mn with the Mn(III) accumulation, especially on the surface 10 nm layer of MnO_x (Fig. 6), both contributing to the layer-to-tunnel transformation of MnO_x in the following stage.

With the layer-to-tunnel MnO_x transformation, Tl would be either incorporated into the tunnel MnO_x or fixed inside the tunnel of MnO_x (Week 4–8), as evidenced by STEM-HAADF (Fig. 4). Mn(III) formation is the prerequisite for the Tl incorporation or fixation for the electron balance (Ruiz-Garcia et al., 2021; Wick et al., 2019), and Tl in both forms was stabilized with the Tl–O–Mn bonding. Tl incorporation should be the primary process, as most of the Tl can only be extracted by high-stability MnO_x dissolution (Fig. 3), accounting for its low mobility and bioaccessibility. The dramatically changing stage of Tl and MnO_x is aligned with the decreased coordination of Tl–Tl, Tl–O, and Tl–Mn path (Table 2).

The crystallization of the tunnel MnO_x with a well-formed structure

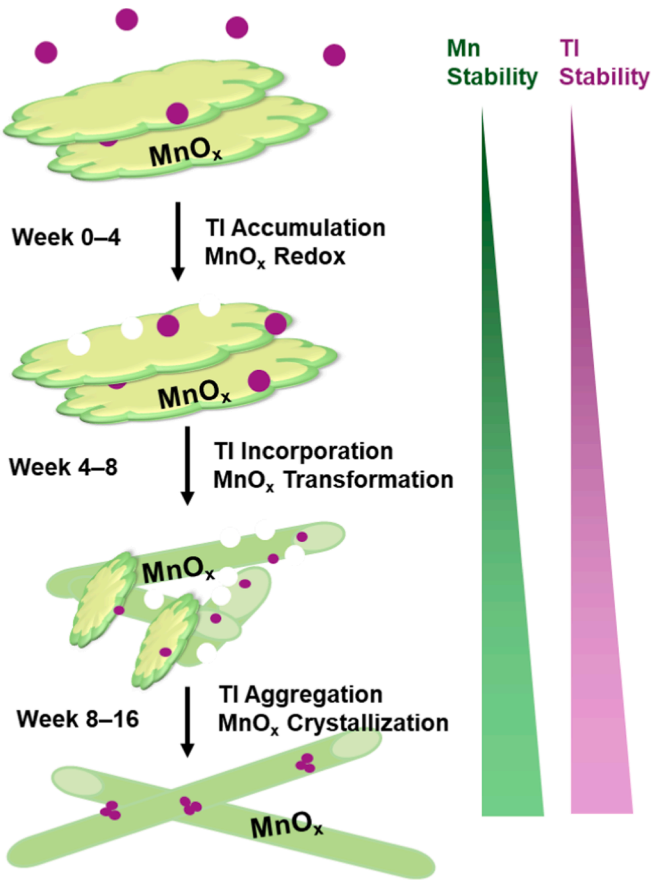

Fig. 7. Fate of Tl during the MnO_x transformation. Stage I: Tl accumulation with Mn redox transformation; Stage II: Tl incorporation with the layer-to-tunnel transformation of MnO_x; Stage III: Tl aggregation with MnO_x crystallization. Tl and Mn stability increased during this three-stage transformation.

was the primary reaction during the final stage (Week 8–16). The shaper peaks in XRD (Fig. 1), signals in the SAED pattern (Appendix S8), increased coordination numbers by EXAFS fitting (Fig. 5), and well tunnel-like structure under HR-TEM (Fig. 4) all support these findings. Less valence transformation of Mn and Tl occurred in this stage, and Tl (I) with Mn(III)/Mn(II) remained as the main species, indicating the potential forms as Tl(I)Mn(III)O_2 (Ruiz-Garcia et al., 2021). Notably, Tl atoms fixed in the tunnel would aggregate with the formation of clusters as detected by the STEM-HAADF. The lattice expansion of MnO_x with an increased distance from 3.19 Å to 3.31 Å could support this conclusion (Appendix S8). In addition, the increased signal of the Tl–Tl path with shorter radium during the final stage of incubation indicated the recombination of Tl within the tunnel of MnO_x (Table 2).

The increasing stability mainly occurred in the first eight weeks of incubation, indicating that both the accumulation and incorporation of Tl contribute to the increasing stability to resist the reductive dissolution by organic acids. The increasing stability of MnO_x with the formation of tunnel MnO_x was crucial to resist the reductive dissolution, leading to the higher stability of incorporated Tl to resist the extraction. In addition, the continuous accumulation of Tl in the high-stability MnO_x was found during the incubation process, especially for MnO_x with PC400 and Tl(III). The Tl/Mn molar ratio in the low-stability MnO_x decreased from 1.88×10^{-3} to 0.57×10^{-3} during the incubation with PC400 and Tl(III), and the Tl/Mn ratio in high-stability MnO_x increased from 2.45×10^{-3} to 3.34×10^{-3}, serving as the direct evidence for the Tl accumulation in stable tunnel MnO_x (Appendix S11). The accumulation of Tl mainly occurred in the first eight weeks, fitting well with the stability variation and transformation stage. By contrast, further crystallization of MnO_x in the last 8 weeks and the Tl accumulation showed a less significant impact on the overall Tl mobility than in the first 8 weeks.

Notably, we found the atomic dispersion of Tl within the 2×2 tunnel of the MnO_x after 4–8 weeks of incubation and its further aggregation with the formation of atomic clusters at the end of 16 weeks. The atomic level distribution of Tl was first reported with MnO_x, and they would be crucial for the geochemistry process. Metal distributed as single atoms and/or atomic clusters at the sub-nano level exhibits significantly higher reactivity than bulk minerals for generating radicals or undergoing direct redox processes (Guo et al., 2022; Rong et al., 2020). Therefore, it is crucial to consider the potential formation and aggregation of metal at the sub-nano level during the layer-to-tunnel MnO_x transformation when interpreting biogeochemical processes, especially for co-existing metals such as iron (Fe) that are highly reactive and abundant in soil.

4.2. *Fast MnO_x transformation induced by the cooperation of redox components*

By comparing MnO_x transformation with different PC and Tl, an apparent mineral transformation can only be found with PC400 and Tl (III) within a short incubation time. A relatively smaller amount of tunnel MnO_x occurred after a long-term incubation with PC700 and Tl (III), implying that PC400 showed a higher potential to trigger the layer-to-tunnel transformation. A higher electron-donating capacity (0.71 mmol e^- g^{-1} > 0.40 mmol e^- g^{-1}) with a lower electron-accepting capacity (0.53 mmol e^- g^{-1} < 0.67 mmol e^- g^{-1}) was detected for the PC400 than PC700 through the electrochemical methods (Xu et al., 2022a) (Fig. 8**a**). The higher reducing capacity of PC400 would be dominant for the layer-to-tunnel transformation, as the reductive formation of Mn(III) was considered as the launching step (Yang et al., 2018).

Unlike the current literature, we observed that only Tl(III) could induce the layer-to-tunnel transformation process with PC, while no detectable evaluation of MnO_x was found with Tl(I) through spectroscopy and extraction evaluation. In other words, reductive Tl(I) negatively impacted the layer-to-tunnel MnO_x transformation with PC. This difference could be attributed to the environmental conditions, as the reported layer-to-tunnel transformation of MnO_x with sole Tl(I) required a high Tl concentration (Tl/Mn = 0.08, *i.e.,* high reducing moiety content) and acidity (pH = 4.0) for the formation of Mn(II)/Mn(III) to induce the MnO_x transformation (Ruiz-Garcia et al., 2021; Wick et al., 2019). This condition could hardly be achieved in soil environment and was different from our studied settings ((Tl/Mn ratio = ~0.002) and mild acidity (pH = ~6.5–7.6)). Under more realistic conditions, the formation of tunnel MnO_x required the contribution from the Tl(III) together with the reductants, *i.e.,* cooperation from reducing and oxidizing components. We calculated the electron exchange capacity of Tl and PC for Mn in different incubation systems (Fig. 8**b**), and the results again confirmed that the suitable cooperation of reducing and oxidizing moieties (*i.e.,* reductive PC with oxidative Tl with EDC/EAC approaching 1) determined the sufficient MnO_x transformation.

Based on the XPS analysis, the reduction of Mn on the surface of MnO_x occurred during the first 8 weeks, which was driven by the pyrogenic carbon, *i.e.,* PC($2e^-$) + Mn(IV) → PC + Mn(II). Meanwhile, the reduction of Tl(III) occurred (Fig. 6), which was related to either direct reduction by PC or electron transfer with Mn(II), *i.e.,* Tl(III) + 2Mn(II) → Tl(I) + 2Mn(III). As the Tl was strongly combined with the MnO_x through Tl–O–Mn bonding, the electron was more likely to be transferred through MnO_x with Mn(II) oxidation to Mn(III). This electron

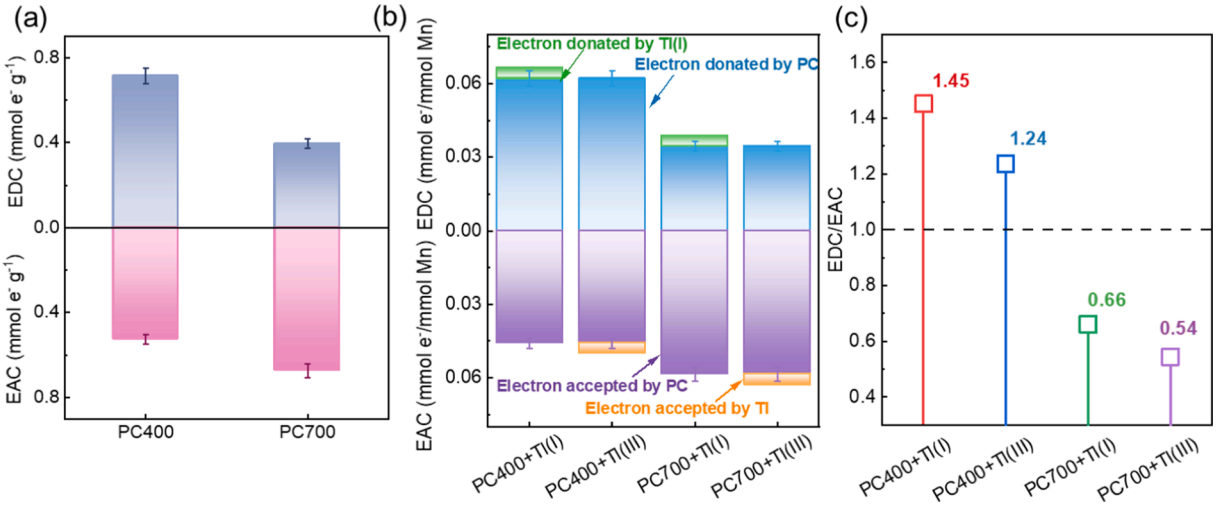

Fig. 8. Electron-donating capacity (EDC) and electron-accepting capacity (EAC) of different PC (a); The redox capacity in different incubation systems (b); the ratio of EDC and EAC in different incubation systems (c).

transfer through redox-active minerals was reported in the Fe minerals to indirectly reduce the combined Cr(VI) by PC (Xu et al., 2022b). The indirect electron transfer process was supported by the Mn oxidation and Tl reduction in the deeper area of MnO_x (10–50 nm), as PC can hardly interact with the Tl inside the MnO_x. Additionally, the limited formation of tunnel MnO_x in the presence of Tl(I) and PC 400 indicated a preference for indirect electron transfer, as opposed to direct electron transfer between PC400 and Tl(III). If Tl(III) were to be reduced by PC400 and subsequently sorbed onto the MnO_x, we would anticipate observing a comparable formation of tunnel MnO_x when contrasting PC400 with Tl(I) and PC400 with Tl(III). In short, the cyclic transformation of Mn was constructed with the reducing capacity of PC and oxidizing capacity of Tl(III) (*i.e.,* PC → MnO_x → Tl (III)), which could be dominant for the layer-to-tunnel transformation of MnO_x.

The average oxidation state of the Mn was approaching three during the first 4 weeks of incubation with Tl(III)-PC400 (Fig. 6**a**), and the surface Mn after 16 weeks of incubation with Tl(III)-PC400 was closer to three compared to other incubation system (Fig. 6**d**). Both results indicated that the cyclic transformation of Mn with PC400 and Tl(III) supported the accumulation of Mn(III) in the whole MnO_x. The Mn(III) formation could benefit from the formation of $Mn(III)Tl(I)O_2$ with a balanced charge during the oxidation of Mn(II) by Tl(III). Mn(III) was a key to the tunnel MnO_x formation, as it would weaken the Mn–O–Mn boundaries to form the nucleus of the tunnel structures (Yang et al., 2018). Moreover, the cyclic transformation of Mn would be responsible for generating surface defects and/or Mn vacancies on the MnO_x with reductive dissolution and oxidative precipitation, which is critical for the topotactic variation of MnO_x (Yang et al., 2018). The high-resolution ACTEM confirmed the formation of structure defects and vacancies on the MnO_x during the incubation with PC and Tl(III) (Fig. 4). In addition, the increasing σ^2 from the shell-by-shell fitting of Mn EXAFS results indicated the increasing disorder degree of the MnO_x during incubation (Table 1). Notably, this cyclic transformation mainly occurred in the first four weeks, accumulating sufficient Mn(III) and vacancies on MnO_x at the end of four weeks (Fig. 6**a**), leading to the next stage of layer-to-tunnel transformation.

The importance of Mn's cyclic valence transformation to the layer-to-tunnel transformation could be verified by using an electrochemical approach (Jung et al., 2020), who found that the formation of hollandite required a higher energy barrier with faster redox cycles. In this study, this was provided by the cooperation of PC400 and Tl(III). The cyclic transformation of Mn could occur during the interactions with small organic carbon (*e.g.,* formic acid, formaldehyde, and methanol) and O_2, driving the biogeochemical cycling of variable valence elements (Ye

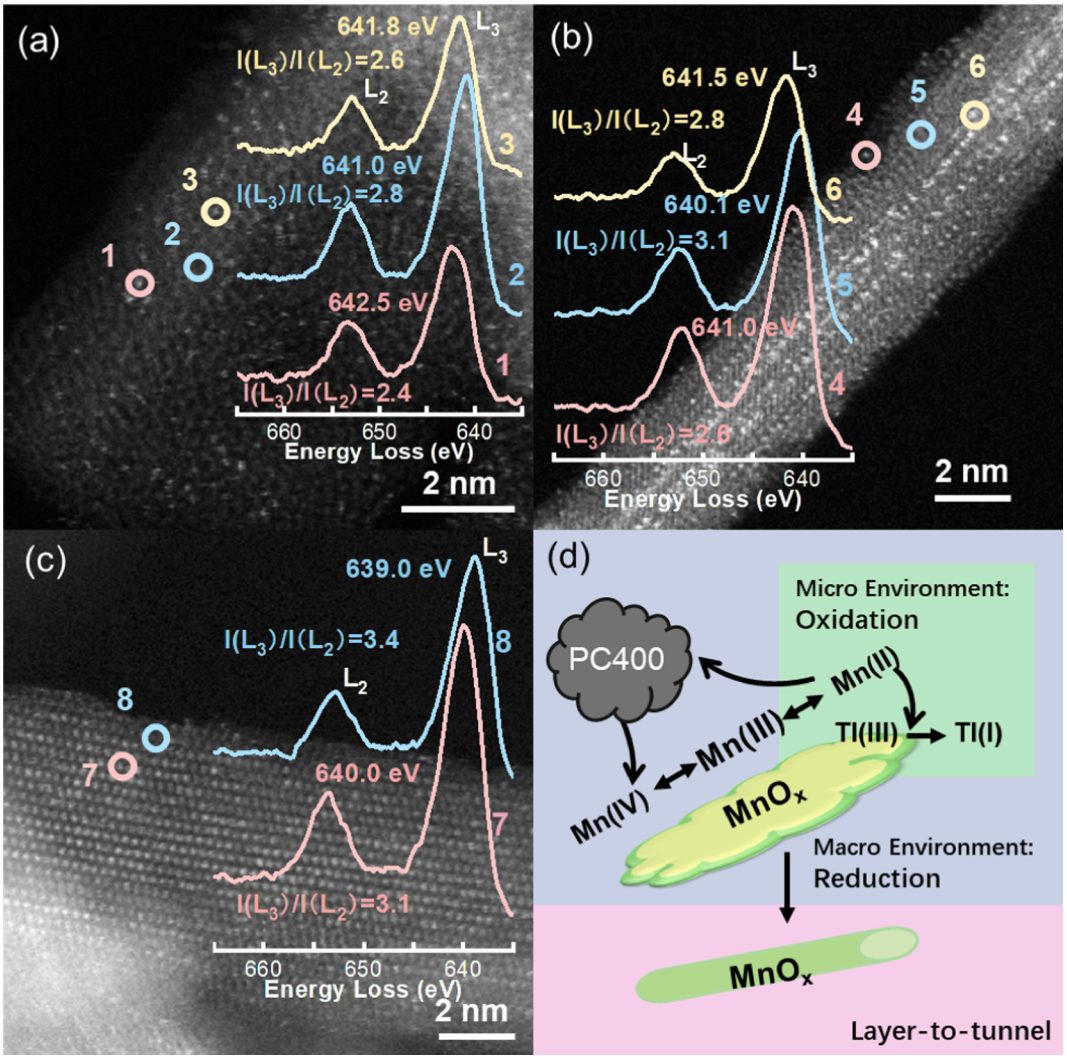

Fig. 9. ACTEM-EELS analysis of MnO_x after 4-week (a), 8-week (b), and 16-week (c) of incubation. The figure insert was the EELS spectrum for the corresponding test points in the enlarged ACTEM-HAADF image. The shown data was the position of Mn-L_3 peaks and the intensity ratio between L_3 and L_2 peaks. Mn reduction occurred during the PC incubation, while chelation with Tl(III) caused the oxidation of Mn with a bigger peak position and lower intensity ratio. The schematic diagram of the electron transfer for the MnO_x transformation (d).

et al., 2024) and mineral transformation.

4.3. Tl(III) chelation for the efficient electron accepting and mineral transformation

According to the EXAFS fitting and TEM evaluation, Tl was strongly chelated on the MnO_x with Tl–O–Mn at the atomic level, which probably created a microenvironment with a relatively high oxidation potential in the inner area of MnO_x. The incorporation and chelation of MnO_x avoided the fast reductive formation of Tl(I) through interaction with PC. TEM-EELS analysis was conducted to evaluate the electron transfer route under the sub-nanoscale level (Fig. 9). The reductive transformation of MnO_x induced by the PC can be evidenced by the redshift of peaks (641.0–642.5 eV > 640.1–641.5 eV > 639.0–640.0 eV) and the increasing intensity ratio of L_3 to L_2 peaks (3.1–3.4 > 2.6–3.1 > 2.4–2.8) (Inoué et al., 2019; Tan et al., 2012) with the increased incubation time with PC. With the attachment of Tl on the MnO_x, the oxidative transformation of Mn was shown with a blueshift of the L_3 peaks (639.0–641.0 eV < 640.0–642.5 eV) compared to the MnO_x area without Tl (Fig. 9). The sub-nanoscale level evaluation of the Mn valence state indicated that the attachment of Tl would induce an oxidative environment in the micro area, thus facilitating the oxidative transformation of Mn.

The importance of the micro oxidation environment created by Tl (III) can be evidenced by the MnO_x transformation with PC alone. A much slower formation of tunnel MnO_x with a higher disorder degree and smaller tunnel size was detected with PC alone; even though PC itself can serve as both electron-donating and accepting moieties (Klüpfel et al., 2014). The more efficient electron withdrawal of the chelated Tl(III) would lead to a faster MnO_x transformation compared to the oxidation by PC. In addition, the limited transformation of MnO_x with soluble reductants and oxidants (*i.e.,* Mn(II) and Tl(III) or Tl(I) and Fe(III)) implied the importance of the micro oxidation environment (Appendix S12). The fast redox reaction between reductants and oxidants in the solution phase (*i.e.,* Mn(II) and Tl(III)) inhibited the formation of a micro oxidation environment and macro reduction environment, resulting in only limited mineral transformation. Another advantage of the Tl chelation was the direct inner electron transfer (instead of electron transfer from the surface to the inner area), leading to a faster Mn valence state cycle (Ye et al., 2024). The atomic dispersion of Tl with MnO_x would impart a higher reactivity, leading to a rapid electron acceptance from Mn(II) with the formation of Mn(III). Tl chelation could regulate the tunnel size as the bridging cations, and it was fixed into the tunnel in the meantime. The efficient electron transfer with the chelated Tl(III) explains the limited transformation with the Tl (I) system, as chelated Tl(I) can only donate instead of accept electrons from the MnO_x directly.

In conclusion, the Tl attachment created an oxidative microenvironment with efficient electron withdrawal, which constructed the oxidation side together with the macro reduction environment related to the PC (Fig. 9**d**). The co-existence of micro oxidation environment and macro reduction environment is a key to forming Mn(III) and layer-to-tunnel transformation of MnO_x.

4.4. Implications on the fate of MnO_x and toxic elements after wildfire

During high-severity wildfires, soil temperature may exceed 600℃ (Rein et al., 2008), leading to mineral transformation and formation of pyrogenic carbon (Lopez et al., 2024; Lopez et al., 2023). Previous studies indicated the transformation of phyllo-manganate to tecto-manganate (cryptomelane) over 400℃, while incorporating metal elements may inhibit this transformation with a high proportion of the birnessite (Yin et al., 2022; Yin et al., 2024). Phyllo-manganate with a highly disordered phase would still be the dominant phase without tunnel MnO_x formation under 400℃ (Golden et al., 1986), a common situation of wildfires with relatively low severity. These disordered MnO_x had a higher chance of getting involved in the layer-to-tunnel transformation with the generated PC. The higher reducing capacity of PC formed under a lower temperature (400℃) and the Tl(III) formed by thermal oxidation could support the cyclic transformation of MnO_x and facilitate its transformation. In short, high-severity wildfires led to the direct topotactic transformation of MnO_x, while low-severity wildfires and post-fire incubation with PC would determine the fate of MnO_x and coexisting toxic elements.

Regarding the toxic elements with MnO_x, the thermal transformation of MnO_x under high temperatures (> 500℃) would significantly increase the stability of attached toxic elements during reductive acid dissolution due to its incorporation into the MnO_x framework (Yin et al., 2022). By contrast, a limited change in the stability of toxic elements occurred under a relatively lower temperature (< 400℃), while our results indicated that their bioaccessibility could be significantly increased during the post-fire incubation with PC. Notably, the limited transformation of birnessite and the attached toxic elements occurred under ambient conditions (*e.g.,* 8-year dry aging under room temperature) (Yin et al., 2022), further emphasizing the critical contribution of wildfire and PC on the fate of minerals and toxic elements. Considering both the direct impact of wildfire and the post-fire incubation with PC is important to provide a comprehensive understanding of wildfire's environmental and geochemical implications.

4.5. Geochemistry implications on pyrogenic carbon

This study highlights the significant role of pyrogenic carbon in initiating the layer-to-tunnel transformation of MnO_x, a crucial geochemical process that provides insights into the behavior of manganese minerals. The geochemistry process initiated by the emergence of pyrogenic carbon has garnered significant attention, primarily due to its substantial soil accumulation (Bowring et al., 2022). Previously reported mineral transformation induced by pyrogenic carbon mainly focused on the Fe minerals or transition metals on the clay minerals (Dong et al., 2023; Xu et al., 2021; Xu et al., 2022b). This study unveiled that sole PC could trigger the layer-to-tunnel Mn transformation with the formation of tunnel Mn with 1×2 or 1×1 size, and the formation of hollandite with 2×2 tunnel size occurred with the support of Tl(III).

The tunnel MnO_x formation inevitably impacts the soil element turnover. The leachability and mobility of the associated toxic elements would be greatly affected (Li et al., 2024), such as Tl (this study), Co (Zhao et al., 2023), Ni (Yin et al., 2022), and Sb (Karimian et al., 2021b), due to their accumulation and incorporation into the tunnel MnO_x with higher stability and lower bioaccessibility. In addition, the redox potential of the tunnel MnO_x differs from the layer MnO_x, thus affecting the redox-sensitive pollutants. These immobilization implications support the pyrogenic carbon application during soil restoration and remediation. Pyrogenic carbon (or biochar) is often considered an adsorbent for pollutants (Ahmad et al., 2014) and redox moieties to reduce the mobility and toxicity of specific elements (*e.g.,* Cr(VI)) (Xu & Tsang, 2022; Xu et al., 2021). This study reveals a new immobilizing route of biochar for pollution control, *i.e.,* triggering the Mn minerals transformation with toxic elements incorporation.

The transformation of Mn minerals has a substantial impact on the fate of soil organic carbon and nutrients (Brüggenwirth et al., 2024; Li et al., 2021), which are related to carbon sequestration and soil conditioning. The influence of pyrogenic carbon on Mn minerals transformation demands attention as a distinct advantage for its wider consideration. The reported MnO_x transformation with elements turnover is crucial for soil revegetation after wildfires, as a certain amount of pyrogenic carbon would be generated during the wildfires (Bodí et al., 2014; Lopez et al., 2023). Our findings serve as a critical reference for these aspects, and more studies are warranted in the future.

4.6. Geochemical implications on the fate of MnO_x

MnO_x represents a potent group of mineral oxidants in soil, and its speciation is crucial for the co-existing elements. In addition to the Mn (II)-induced transformation of MnO_x with the assistance of reductants, this study proposed that the cooperation of reductants and oxidants could further facilitate the layer-to-tunnel transformation of MnO_x. The key was the chelation of oxidants (*i.e.,* Tl(III)) on MnO_x to create a micro oxidation environment under the macro reduction environment.

Other cationic elements, such as Co (Wu et al., 2019a, 2019b), Ni (Wu et al., 2020), and Fe (Yin et al., 2013), with an oxidation potential may contribute to the layer-to-tunnel transformation of MnO_x together with the PC. A wide range of cationic metals can be anchored on the MnO_x, forming stable surface complexes, and most contain a variable valence state with potential as an oxidizing agent. For instance, we also observed the formation of tunnel MnO_x with 2 × 2, 1 × 2, and 1 × 1 tunnels with Fe/Ni and PC after 16 weeks of incubation (Appendix S12). Further investigation is needed to understand the actual control of tunnel size, which might be related to the proportion of Mn(III), atomic size of the cations, and frequency of redox cycles. The formation of todorokite (3 × 3 tunnel size), non-ideal 3 × n tunnel MnO_x (Wu et al., 2019a, 2019b), or even 4 × 4 tunnel MnO_x (Yang et al., 2018) was reported. The key issues that are controlling the tunnel size are still underexplored. Oxyanions, especially CrO_4^{2-}, might have a potential capacity to serve as oxidants to trigger the layer-to-tunnel MnO_x transformation together with the reductants, while relevant studies are limited.

We used pyrogenic carbon as the reductant to trigger the layer-to-tunnel transformation, while other reductants, including soil organic matter, Fe(II), Mn(II), and toxic elements, can potentially serve as the reduction sites for the pairwise redox components. Cooperation of As (III)–Fe(III) (Mock et al., 2019), Fe(II)–Cr(VI) (Liao et al., 2019), Fe(II)–O_2 (van Genuchten & Ahmad, 2020), organic matter–Fe(III) (Patzner et al., 2020; Xu et al., 2022b), Mn(II)–Sb(V) (Karimian et al., 2021a), organic matter–O_2 (Ye et al., 2024), and organic matter-Mn(IV) (Trainer et al., 2021) can be found in the soil environment. Their cooperation might trigger similar tunnel MnO_x formation, while their direct interactions would affect the cyclic valence transformation of Mn(IV).

Tunnel MnO_x was also formed when incubated with Fe(III)/Tl(I) or Tl(III)/Mn(II) as the redox components, but the formation was less apparent compared to the PC system (Appendix S12). This could be attributed to the fast interaction between Tl(III) and Mn(II) in the solution without interactions with MnO_x. The soluble phase of PC was extracted and incubated with the MnO_x together with Tl(III) and/or Fe (III), and a limited extent of transformation occurred (Appendix S12). The soluble phase of PC contained a lower reducing capacity to trigger the reduction process (Xu et al., 2022b), and they could quickly interact with soluble ions instead of the MnO_x. Sorption of elements on the PC is the first step for the electron transfer process, thus allowing the oxidative species to interact with MnO_x and create a micro oxidative environment to foster the cyclic Mn valence transformation. In short, the layer-to-tunnel transformation of MnO_x can be triggered by PC and a wide range of oxidative elements, while how to ensure the cyclic transformation of Mn by pairwise interactions with both reductants and oxidants is key to the transformation process.

In addition, the dynamic nature of soil systems, including sequential flooding and draining, can alter the redox potential and lead to the coexistence of reducing and oxidizing species in the soil. The transition zone between oxygen-rich and oxygen-deficient conditions, such as in wetland and paddy soil, can create a gradient of reduction potential within a short distance, exposing the soil to oxidizing and reducing conditions (Madison et al., 2013). Further studies are needed to scrutinize the electron transfer and MnOx transformation under these dynamic conditions.

5. Conclusions

In this study, we investigated the layer-to-tunnel transformation of MnO_x with the coexistence of pyrogenic carbon and Tl. The results showed that the formation of hollandite (tunnel MnO_x with 2 × 2 tunnel size) only occurred with PC and Tl(III), while Tl(I) failed to induce the MnO_x transformation with or without PC. The macro reducing environment created by the PC and the micro oxidizing environment related to the locally chelated Tl(III) was pivotal in forming the active Mn(III) species and structure vacancies on MnO_x, which were the prerequisites for its layer-to-tunnel transformation through the cyclic electron transfer process. This finding advances our understanding related to the tunnel MnO_x formation, as the cooperation of reducing and oxidizing components can trigger the MnO_x transformation under mild conditions, which sole reductants cannot achieve. The crystal tunnel MnO_x formation can incorporate the chelated Tl into the tunnel, resulting in the high stability and low bioaccessibility of Tl. Our results emphasize the critical roles of cooperation of electron-donating and electron-accepting components in triggering MnO_x transformation, which has significant implications for understanding the fate of carbon, minerals, and toxic elements in the environment.

CRediT authorship contribution statement

Zibo Xu: Writing – original draft, Visualization, Validation, Methodology, Investigation, Formal analysis, Conceptualization. **Bin Ma:** Writing – review & editing, Validation, Investigation. **Yuanzhi Tang:** Writing – review & editing, Validation, Investigation. **Daniel C.W. Tsang:** Writing – review & editing, Supervision, Project administration, Investigation, Funding acquisition, Conceptualization.

Declaration of competing interest

The authors declare that they have no known competing financial interests or personal relationships that could have appeared to influence the work reported in this paper.

Acknowledgment

The authors appreciate the financial support from the Hong Kong Research Grants Council (HKUST 15231522), Hong Kong Environment and Conservation Fund (ECF Project 95/2023), and HKUST '30 for 30' Global Talent Acquisition Campaign.

Appendix A. Supplementary material

The supplementary materials, including the mediated electrochemical approach (Appendix S1), change of pH during the incubation (Appendix S2), XAS analysis (Appendix S3), extraction methods to evaluate the Tl/Mn speciation (Appendix S4), Evaluation methods for the bioaccessibility and leachability of Tl/Mn (Appendix S5), Mn and Tl variation in solution and soil (Appendix S6&S7), HR-TEM-SAED analysis (Appendix S8), morphology evaluation during incubation (Appendix S9), XPS analysis (Appendix S10), Tl/Mn ratios (Appendix S11), and MnOx transformation in different incubation system (Appendix S12) can be found online. Supplementary material to this article can be found online at https://doi.org/10.1016/j.gca.2024.11.015.

References

Ahmad, M., Rajapaksha, A.U., Lim, J.E., Zhang, M., Bolan, N., Mohan, D., Vithanage, M., Lee, S.S., Ok, Y.S., 2014. Biochar as a sorbent for contaminant management in soil and water: a review. Chemosphere 99, 19–33.

Aiken, M.L., Abernathy, M.J., Schaefer, M.V., Lee, I., Ying, S.C., 2023. Inhibition of chromium(III) oxidation through manganese(IV) oxide passivation and iron(II) abiotic reduction. ACS Earth Space Chem. 7 (12), 2327–2338.

Atkins, A.L., Shaw, S., Peacock, C.L., 2016. Release of Ni from birnessite during transformation of birnessite to todorokite: implications for Ni cycling in marine sediments. Geochim. Cosmochim. Acta 189, 158–183.
Bodí, M.B., Martin, D.A., Balfour, V.N., Santín, C., Doerr, S.H., Pereira, P., Cerdà, A., Mataix-Solera, J., 2014. Wildland fire ash: production, composition and eco-hydro-geomorphic effects. Earth-Sci. Rev. 130, 103–127.
Bowring, S.P.K., Jones, M.W., Ciais, P., Guenet, B., Abiven, S., 2022. Pyrogenic carbon decomposition critical to resolving fire's role in the Earth system. Nat. Geosci. 15 (2), 135–142.
Brüggenwirth, L., Behrens, R., Schnee, L.S., Sauheitl, L., Mikutta, R., Mikutta, C., 2024. Interactions of manganese oxides with natural dissolved organic matter: Implications for soil organic carbon cycling. Geochim. Cosmochim. Acta 366, 182–200.
Chen, P., Zhou, Y., Xie, Q., Chen, T., Liu, H., Xue, S., Zou, X., Wei, L., Xu, L., Zhang, X., Rosso, K.M., 2022. Phosphate adsorption kinetics and equilibria on natural iron and manganese oxide composites. *J. Environ. Manage.* 323, 116222.
Cruz-Hernández, Y., Ruiz-García, M., Villalobos, M., Romero, F.M., Meza-Figueroa, D., Garrido, F., Hernández-Alvarez, E., Pi-Puig, T., 2018. Fractionation and mobility of thallium in areas impacted by mining-metallurgical activities: Identification of a water-soluble Tl(I) fraction. *Environ. Pollut.* 237, 154–165.
Cruz-Hernández, Y., Villalobos, M., Marcus, M.A., Pi-Puig, T., Zanella, R., Martínez-Villegas, N., 2019. Tl(I) sorption behavior on birnessite and its implications for mineral structural changes. *Geochim. Cosmochim. Acta* 248, 356–369.
Dong, H., Coffin, E.S., Sheng, Y., Duley, M.L., Khalifa, Y.M., 2023. Microbial reduction of Fe(III) in nontronite: Role of biochar as a redox mediator. *Geochim. Cosmochim. Acta* 345, 102–116.
Du, J., Kim, K., Son, S., Pan, D., Kim, S., Choi, W., 2023. MnO_2-induced oxidation of iodide in frozen solution. *Environ. Sci. Tech.* 57 (13), 5317–5326.
Du, Y., Shi, L., Li, X., Liu, J., Ying, R., Hu, P., Wu, L., Christie, P., 2024. Potential mobilization of water-dispersible colloidal thallium and arsenic in contaminated soils and sediments in mining areas of southwest China. *J. Hazard. Mater.* 465, 133211.
Elzinga, E.J., 2011. Reductive transformation of birnessite by aqueous Mn(II). *Environ. Sci. Tech.* 45 (15), 6366–6372.
Flynn, E.D., Catalano, J.G., 2019. Reductive transformations of layered manganese oxides by small organic acids and the fate of trace metals. *Geochim. Cosmochim. Acta* 250, 149–172.
Golden, D.C., Dixon, J.B., Chen, C.C., 1986. Ion exchange, thermal transformations, and oxidizing properties of birnessite. *Clay Clay Miner.* 34 (5), 511–520.
Guo, Y., Wang, M., Zhu, Q., Xiao, D., Ma, D., 2022. Ensemble effect for single-atom, small cluster and nanoparticle catalysts. *Nat. Catal.* 5 (9), 766–776.
Hu, E., Pan, S., Zhang, W., Zhao, X., Liao, B., He, F., 2019. Impact of dissolved O_2 on phenol oxidation by δ-MnO2. *Environ. Sci. Processes Impacts* 21 (12), 2118–2127.
Inoué, S., Yasuhara, A., Ai, H., Hochella, M.F., Murayama, M., 2019. Mn(II) oxidation catalyzed by nanohematite surfaces and manganite/hausmannite core-shell nanowire formation by self-catalytic reaction. *Geochim. Cosmochim. Acta* 258, 79–96.
IUSS Working Group. 2014. World reference base for soil resources 2014. International soil classification system for naming soils and creating legends for soil maps.
Jiang, Y., Wei, X., He, H., She, J., Liu, J., Fang, F., Zhang, W., Liu, Y., Wang, J., Xiao, T., Tsang, D.C.W., 2022. Transformation and fate of thallium and accompanying metal (loid)s in paddy soils and rice: a case study from a large-scale industrial area in China. J. Hazard. Mater. 423, 126997.
Jung, H., Taillefert, M., Sun, J., Wang, Q., Borkiewicz, O.J., Liu, P., Yang, L., Chen, S., Chen, H., Tang, Y., 2020. Redox cycling driven transformation of layered manganese oxides to tunnel structures. *J. Am. Chem. Soc.* 142 (5), 2506–2513.
Karimian, N., Hockmann, K., Planer-Friedrich, B., Johnston, S.G., Burton, E.D., 2021a. Antimonate controls manganese(II)-induced transformation of birnessite at a circumneutral pH. *Environ. Sci. Tech.* 55 (14), 9854–9863.
Karimian, N., Johnston, S.G., Burton, E.D., 2021b. Reductive transformation of birnessite and the mobility of co-associated antimony. *J. Hazard. Mater.* 404, 124227.
Karolewski, J.S., Sutherland, K.M., Hansel, C.M., Wankel, S.D., 2021. An isotopic study of abiotic nitrite oxidation by ligand-bound manganese (III). *Geochim. Cosmochim. Acta* 293, 365–378.
Kluepfel, L., Keiluweit, M., Kleber, M., Sander, M., 2014. Redox properties of plant biomass-derived black carbon (biochar). *Environ. Sci. Tech.* 48 (10), 5601–5611.
Lehmann, J., 2007. A handful of carbon. *Nature* 447 (7141), 143–144.
Lehmann, J., Cowie, A., Masiello, C.A., Kammann, C., Woolf, D., Amonette, J.E., Cayuela, M.L., Camps-Arbestain, M., Whitman, T., 2021. Biochar in climate change mitigation. *Nat. Geosci.* 14 (12), 883–892.
Li, H., Santos, F., Butler, K., Herndon, E., 2021. A critical review on the multiple roles of manganese in stabilizing and destabilizing soil organic matter. *Environ. Sci. Tech.* 55 (18), 12136–12152.
Li, F., Yin, H., Zhu, T., Zhuang, W., 2024. Understanding the role of manganese oxides in retaining harmful metals: insights into oxidation and adsorption mechanisms at microstructure level. *Eco-Environ. Health* 3 (1), 89–106.
Liao, W., Ye, Z., Yuan, S., Cai, Q., Tong, M., Qian, A., Cheng, D., 2019. Effect of coexisting Fe(III) (oxyhydr)oxides on Cr(VI) reduction by Fe(II)-bearing clay minerals. *Environ. Sci. Tech.* 53 (23), 13767–13775.
Limmer, M.A., Linam, F.A., Evans, A.E., Seyfferth, A.L., 2023. Unraveling the mechanisms of Fe oxidation and Mn reduction on Mn indicators of reduction in soil (IRIS) films. *Environ. Sci. Tech.* 57 (16), 6530–6539.
Lis, J., Pasieczna, A., Karbowska, B., Zembrzuski, W., Lukaszewski, Z., 2003. Thallium in soils and stream sediments of a Zn−Pb mining and smelting area. *Environ. Sci. Tech.* 37 (20), 4569–4572.
Liu, J., Wang, J., Tsang, D.C.W., Xiao, T., Chen, Y., Hou, L., 2018. Emerging thallium pollution in china and source tracing by thallium isotopes. *Environ. Sci. Tech.* 52 (21), 11977–11979.
Liu, J., Luo, X., Sun, Y., Tsang, D.C.W., Qi, J., Zhang, W., Li, N., Yin, M., Wang, J., Lippold, H., Chen, Y., Sheng, G., 2019. Thallium pollution in China and removal technologies for waters: a review. *Environ. Int.* 126, 771–790.
Liu, J., Inoué, S., Zhu, R., He, H., Hochella, M.F., 2021. Facet-specific oxidation of Mn(II) and heterogeneous growth of manganese (oxyhydr)oxides on hematite nanoparticles. *Geochim. Cosmochim. Acta* 307, 151–167.
Liu, J., Yuan, W., Lin, K., Wang, J., Sonne, C., Rinklebe, J., 2023. Thallium pollution from the lithium industry calls for urgent international action on regulations. *Environ. Sci. Tech.* 57 (48), 19099–19101.
Lopez, A.M., Pacheco, J.L., Fendorf, S., 2023. Metal toxin threat in wildland fires determined by geology and fire severity. *Nat. Commun.* 14 (1), 8007.
Lopez, A.M., Avila, C.C.E., VanderRoest, J.P., Roth, H.K., Fendorf, S., Borch, T., 2024. Molecular insights and impacts of wildfire-induced soil chemical changes. *Nat. Rev. Earth Environ.* 5 (6), 431–446.
Madison, A.S., Tebo, B.M., Mucci, A., Sundby, B., Luther, G.W., 2013. Abundant porewater mn(iii) is a major component of the sedimentary redox system. *Science* 341 (6148), 875–878.
Manceau, A., Steinmann, S.N., 2023. Density Functional Theory modeling of the oxidation mechanism of Tl(I) by birnessite. *ACS Earth Space Chem.* 7 (7), 1459–1466.
Marafatto, F.F., Dähn, R., Grolimund, D., Göttlicher, J., Voegelin, A., 2021. Thallium sorption by soil manganese oxides: Insights from synchrotron X-ray micro-analyses on a naturally thallium-rich soil. *Geochim. Cosmochim. Acta* 302, 193–208.
Mock, R.P., Schaefer, M.V., Pacheco, J.L., Lake, L., Lee, I., Ying, S.C., 2019. Influence of Fe(II) on Arsenic(III) oxidation by birnessite in diffusion-limited systems. *ACS Earth Space Chem.* 3 (4), 550–561.
Moore, O.W., Curti, L., Woulds, C., Bradley, J.A., Babakhani, P., Mills, B.J.W., Homoky, W.B., Xiao, K.-Q., Bray, A.W., Fisher, B.J., Kazemian, M., Kaulich, B., Dale, A.W., Peacock, C.L., 2023. Long-term organic carbon preservation enhanced by iron and manganese. *Nature* 621 (7978), 312–317.
Patzner, M.S., Mueller, C.W., Malusova, M., Baur, M., Nikeleit, V., Scholten, T., Hoeschen, C., Byrne, J.M., Borch, T., Kappler, A., Bryce, C., 2020. Iron mineral dissolution releases iron and associated organic carbon during permafrost thaw. *Nat. Commun.* 11 (1), 6329.
Peacock, C.L., Moon, E.M., 2012. Oxidative scavenging of thallium by birnessite: Explanation for thallium enrichment and stable isotope fractionation in marine ferromanganese precipitates. *Geochim. Cosmochim. Acta* 84, 297–313.
Peter, A.L.J., Viraraghavan, T., 2005. Thallium: a review of public health and environmental concerns. *Environ. Int.* 31 (4), 493–501.
Phillips, R.F., Wang, Y., Klein, F., Farfan, G., Ostrander, C.M., Gadol, H., Hansel, C.M., Nielsen, S.G., 2023. The role of manganese oxide mineralogy in thallium isotopic fractionation upon sorption. *Geochim. Cosmochim. Acta* 356, 83–92.
Post, J.E., 1999. Manganese oxide minerals: Crystal structures and economic and environmental significance. *Proc. Natl. Acad. Sci.* 96 (7), 3447–3454.
Rein, G., Cleaver, N., Ashton, C., Pironi, P., Torero, J.L., 2008. The severity of smouldering peat fires and damage to the forest soil. *Catena* 74 (3), 304–309.
Rong, H., Ji, S., Zhang, J., Wang, D., Li, Y., 2020. Synthetic strategies of supported atomic clusters for heterogeneous catalysis. *Nat. Commun.* 11 (1), 5884.
Ruby, M.V., Davis, A., Schoof, R., Eberle, S., Sellstone, C.M., 1996. Estimation of lead and arsenic bioavailability using a physiologically based extraction test. *Environ. Sci. Tech.* 30 (2), 422–430.
Ruiz-Garcia, M., Villalobos, M., Voegelin, A., Pi-Puig, T., Martínez-Villegas, N., Göttlicher, J., 2021. Transformation of hexagonal birnessite upon reaction with thallium(I): Effects of birnessite crystallinity, pH, and thallium concentration. *Environ. Sci. Tech.* 55 (8), 4862–4870.
Sun, T.R., Levin, B.D.A., Guzman, J.J.L., Enders, A., Muller, D.A., Angenent, L.T., Lehmann, J., 2017. Rapid electron transfer by the carbon matrix in natural pyrogenic carbon. *Nat. Commun.* 8.
Tan, H., Verbeeck, J., Abakumov, A., Van Tendeloo, G., 2012. Oxidation state and chemical shift investigation in transition metal oxides by EELS. *Ultramicroscopy* 116, 24–33.
Trainer, E.L., Ginder-Vogel, M., Remucal, C.K., 2021. Selective reactivity and oxidation of dissolved organic matter by manganese oxides. *Environ. Sci. Tech.* 55 (17), 12084–12094.
van Genuchten, C.M., Ahmad, A., 2020. Groundwater As removal by As(III), Fe(II), and Mn(II) co-oxidation: contrasting As removal pathways with O_2, NaOCl, and $KMnO_4$. *Environ. Sci. Tech.* 54 (23), 15454–15464.
Villalobos, M., Toner, B., Bargar, J., Sposito, G., 2003. Characterization of the manganese oxide produced by pseudomonas putida strain MnB1. *Geochim. Cosmochim. Acta* 67 (14), 2649–2662.
Voegelin, A., Pfenninger, N., Petrikis, J., Majzlan, J., Plötze, M., Senn, A.-C., Mangold, S., Steininger, R., Göttlicher, J., 2015. Thallium speciation and extractability in a thallium- and arsenic-rich soil developed from mineralized carbonate rock. *Environ. Sci. Tech.* 49 (9), 5390–5398.
Wang, Q., Yang, P., Zhu, M., 2018. structural transformation of birnessite by fulvic acid under anoxic conditions. *Environ. Sci. Tech.* 52 (4), 1844–1853.
Wang, Q., Yang, P., Zhu, M., 2019. Effects of metal cations on coupled birnessite structural transformation and natural organic matter adsorption and oxidation. *Geochim. Cosmochim. Acta* 250, 292–310.
Weng, Z., Van Zwieten, L., Tavakkoli, E., Rose, M.T., Singh, B.P., Joseph, S., Macdonald, L.M., Kimber, S., Morris, S., Rose, T.J., Archanjo, B.S., Tang, C., Franks, A.E., Diao, H., Schweizer, S., Tobin, M.J., Klein, A.R., Vongsivut, J., Chang, S.L.Y., Kopittke, P.M., Cowie, A., 2022. Microspectroscopic visualization of how biochar lifts the soil organic carbon ceiling. *Nat. Commun.* 13 (1), 5177.
Wick, S., Peña, J., Voegelin, A., 2019. Thallium sorption onto manganese oxides. *Environ. Sci. Tech.* 53 (22), 13168–13178.

Wick, S., Baeyens, B., Marques Fernandes, M., Göttlicher, J., Fischer, M., Pfenninger, N., Plötze, M., Voegelin, A., 2020. Thallium sorption and speciation in soils: Role of micaceous clay minerals and manganese oxides. *Geochim. Cosmochim. Acta* 288, 83–100.

Wu, Z., Peacock, C.L., Lanson, B., Yin, H., Zheng, L., Chen, Z., Tan, W., Qiu, G., Liu, F., Feng, X., 2019b. Transformation of Co-containing birnessite to todorokite: Effect of Co on the transformation and implications for Co mobility. *Geochim. Cosmochim. Acta* 246, 21–40.

Wu, Z., Lanson, B., Feng, X., Yin, H., Qin, Z., Wang, X., Tan, W., Chen, Z., Wen, W., Liu, F., 2020. Transformation of Ni-containing birnessite to tectomanganate: Influence and fate of weakly bound Ni(II) species. *Geochim. Cosmochim. Acta* 271, 96–115.

Wu, Z., Lanson, B., Feng, X., Yin, H., Tan, W., He, F., Liu, F., 2021. Transformation of the phyllomanganate vernadite to tectomanganates with small tunnel sizes: Favorable geochemical conditions and fate of associated Co. *Geochim. Cosmochim. Acta* 295, 224–236.

Wu, M., Shu, Y., Song, L., Liu, B., Zhang, L., Wang, L., Liu, Y., Bi, J., Xiong, C., Cao, Z., Xu, S., Xia, W., Li, Y., Wang, Y., 2019a. Prenatal exposure to thallium is associated with decreased mitochondrial DNA copy number in newborns: Evidence from a birth cohort study. *Environ. Int.* 129, 470–477.

Xu, Z., Tsang, D.C.W., 2022. Redox-induced transformation of potentially toxic elements with organic carbon in soil. *Carb. Res.* 1 (1).

Xu, Z., Xu, X., Tao, X., Yao, C., Tsang, D.C.W., Cao, X., 2019. Interaction with low molecular weight organic acids affects the electron shuttling of biochar for Cr(VI) reduction. *J. Hazard. Mater.* 378.

Xu, Z., Xu, X., Zhang, Y., Yu, Y., Cao, X., 2020. Pyrolysis-temperature depended electron donating and mediating mechanisms of biochar for Cr(VI) reduction. *J. Hazard. Mater.* 388, 121794.

Xu, Z., Xu, X., Yu, Y., Yao, C., Tsang, D.C.W., Cao, X., 2021. Evolution of redox activity of biochar during interaction with soil minerals: effect on the electron donating and mediating capacities for Cr(VI) reduction. *J. Hazard. Mater.* 414, 125483.

Xu, Z., Wan, Z., Sun, Y., Gao, B., Hou, D., Cao, X., Komarek, M., Ok, Y.S., Tsang, D.C.W., 2022a. Electroactive Fe-biochar for redox-related remediation of arsenic and chromium: distinct redox nature with varying iron/carbon speciation. *J. Hazard. Mater.* 430, 128479.

Xu, Z., Yu, Y., Xu, X., Tsang, D.C.W., Yao, C., Fan, J., Zhao, L., Qiu, H., Cao, X., 2022b. Direct and indirect electron transfer routes of chromium(VI) Reduction with different crystalline ferric oxyhydroxides in the presence of pyrogenic carbon. *Environ. Sci. Tech.*

Yang, P., Lee, S., Post, J.E., Xu, H., Wang, Q., Xu, W., Zhu, M., 2018. Trivalent manganese on vacancies triggers rapid transformation of layered to tunneled manganese oxides (TMOs): Implications for occurrence of TMOs in low-temperature environment. *Geochim. Cosmochim. Acta* 240, 173–190.

Ye, H., Hu, Z., Yin, R., Boyko, T.D., Liu, Y., Li, Y., Li, C., Lu, A., Li, Y., 2024. Electron transfer at birnessite/organic compound interfaces: mechanism, regulation, and two-stage kinetic discrepancy in structural rearrangement and decomposition. *Geochim. Cosmochim. Acta*.

Yin, H., Liu, F., Feng, X., Hu, T., Zheng, L., Qiu, G., Koopal, L.K., Tan, W., 2013. Effects of Fe doping on the structures and properties of hexagonal birnessites – Comparison with Co and Ni doping. *Geochim. Cosmochim. Acta* 117, 1–15.

Yin, H., Lanson, B., Zhang, S., Liu, L., Peacock, C.L., Post, J.E., Zhu, M., Li, W., Wang, Q., Zhang, J., Yang, Y., Qiu, G., Feng, X., Tan, W., Liu, F., 2022. Effect and fate of Ni during aging and thermal-induced phyllomanganate-to-tectomanganate transformation. *Geochim. Cosmochim. Acta* 333, 200–215.

Yin, H., Zhang, S., Xiang, Y., Zuo, W., Hou, J., Zhang, J., Hong, M., Feng, X., Tan, W., Liu, F., 2024. Effects of dry aging and heating on the structural characteristics and transformation of hexagonal turbostratic birnessite. *Soil Sci. Soc. Am. J.* 88 (2), 258–272.

Yuan, Y., He, K., Lu, J., 2024. Structure–property interplay within microporous manganese dioxide tunnels for sustainable energy storage. *Angew. Chem.* 63 (10) e202316055.

Zhang, S., Li, B., Chen, Y., Zhu, M., Pedersen, J.A., Gu, B., Wang, Z., Li, H., Liu, J., Zhou, X.-Q., Hao, Y.-Y., Jiang, H., Liu, F., Liu, Y.-R., Yin, H., 2023. Methylmercury degradation by trivalent manganese. *Environ. Sci. Tech.* 57 (14), 5988–5998.

Zhang, Y., Xu, X., Cao, L., Ok, Y.S., Cao, X., 2018. Characterization and quantification of electron donating capacity and its structure dependence in biochar derived from three waste biomasses. *Chemosphere* 211, 1073–1081.

Zhang, Y., Xu, X., Zhang, P., Ling, Z., Qiu, H., Cao, X., 2019. Pyrolysis-temperature depended quinone and carbonyl groups as the electron accepting sites in barley grass derived biochar. *Chemosphere* 232, 273–280.

Zhao, H., Feng, X., Lee, S., Reinhart, B., Elzinga, E.J., 2023. Sorption and oxidation of Co (II) at the surface of birnessite: impacts of aqueous Mn(II). *Chem. Geol.* 618, 121281.

Zhao, S., González-Valle, Y.A., Elzinga, E.J., Saad, E.M., Tang, Y., 2018. Effect of Zn(II) coprecipitation on Mn(II)-induced reductive transformation of birnessite. *Chem. Geol.* 492, 12–19.